

Volumetric Rendering for Holographic Display of Medical Data

by

Wendy J. Plesniak


Bachelor of Fine Arts
Carnegie-Mellon University
1984

Bachelor of Science in Electrical Engineering
Carnegie-Mellon University
1986


Submitted to the Media Arts and Sciences Section
in Partial Fulfillment of the Requirements for the Degree of
Master of Science
at the Massachusetts Institute of Technology
September 1988

©Massachusetts Institute of Technology 1988
All Rights Reserved

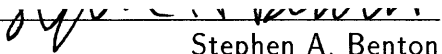
Signature of the Author


Wendy J. Plesniak
Media Arts and Sciences Section
August 5, 1988

Certified by


Stephen A. Benton
Professor of Media Technology
Thesis Supervisor

Accepted by


Stephen A. Benton
Chairman

Departmental Committee on Graduate Students

MASSACHUSETTS INSTITUTE
OF TECHNOLOGY

NOV 03 1988

Rotch
LIBRARIES



Room 14-0551
77 Massachusetts Avenue
Cambridge, MA 02139
Ph: 617.253.2800
Email: docs@mit.edu
<http://libraries.mit.edu/docs>

DISCLAIMER OF QUALITY

Due to the condition of the original material, there are unavoidable flaws in this reproduction. We have made every effort possible to provide you with the best copy available. If you are dissatisfied with this product and find it unusable, please contact Document Services as soon as possible.

Thank you.

Images in this file are the best quality available.

Volumetric Rendering for Holographic Display of Medical Data

by

Wendy J. Plesniak

Submitted to the Media Arts and Sciences Section
in Partial Fulfillment of the Requirements for the Degree of
Master of Science
at the Massachusetts Institute of Technology
September 1988

Abstract

Two factors are fostering the development of three-dimensional (3D) display of medical data. First, the continuing improvement of imaging equipment for medical scanning provides data with higher spatial resolution and increasing signal to noise ratio. Such data lend themselves well to image enhancement and computer-graphic 3D reconstruction algorithms. Secondly, as display technologies improve, different methods are becoming available for displaying these three-dimensional medical data for more complete understanding. Various methods of 3D display are available, such as the varifocal mirror, head-tracked display workstations, and holographic stereograms.

By combining recently-developed volumetric rendering techniques which provide an excellent visualization of the scan data, and holographic stereogram technology, it was hypothesized that the spatial images generated would allow rapid and accurate comprehension of complex volumetric data. In this work, an exploration of holographic display of computer-graphically reconstructed medical data is documented. The implementation of a volumetric rendering algorithm which generates computer graphic images, and the method of recording these images holographically is also documented.

Thesis Supervisor: Stephen A. Benton
Title: Professor of Media Technology

Contents

1	Chapter 1: Introduction	8
2	Chapter 2: Background	12
2.1	Conventional 2D Display of Medical Data	13
2.1.1	Black and White Display Issues	13
2.1.2	Color Display Issues	15
2.2	Methods of 3D Editing and Reconstruction of Medical Data . . .	17
2.2.1	Geometric Rendering Approach	18
2.2.2	Luminous Voxel Method	21
2.2.3	Volume Rendering	22
2.3	2D Display Shortcomings	23
2.4	Role of Three-Dimensional Display in Medical Imaging	23
2.4.1	Cues to Depth	23
2.4.2	Slice Stacking	25
2.4.3	Holographic Display of Medical Data	25
3	Chapter 3: Volume Rendering Analysis	28
3.1	Medical Data Acquisition	29
3.2	Gradients as Surface Normals	32
3.3	Grayscale to Opacity Mapping	34
3.4	Opacity Calculations	37
3.5	Color Calculations	38
4	Chapter 4: Design of Volume Renderer	44

4.1	Overview of the Rendering Process	44
4.2	Ray Tracing	51
4.3	Rendering for Holographic Display	58
5	Chapter 5: Holographic Display of Component Images	62
5.1	Mastering	62
5.2	Transferring	66
5.3	Reconstruction	69
6	Chapter 6: Results	71
6.1	Orthopedic CT	71
6.2	Cardiac MRI	75
6.2.1	Opaque Heart	78
6.2.2	Transparent Heart	82
6.3	Image Quality	88
7	Chapter 7: Conclusions and Future Work	92
8	References	94
9	Bibliography	96

List of Figures

3.1	Average CT and MRI specs, courtesy General Electric Inc.	31
3.2	Gray-level gradients as surface normals.	33
3.3	Idealized histogram plot of CT volume.	35
3.4	Histogram plot of MRI volume.	36
4.1	Array of slices comprising a volume.	45
4.2	Data preprocessing step.	47
4.3	Voxel gray-level gradient calculations.	48
4.4	Voxel opacity calculations.	49
4.5	Rendering Pipeline.	50
4.6	Ray tracing through the volume.	55
4.7	Bilinear interpolation of color and opacity values.	56
4.8	Renderer interface to holographic printer geometry.	59
4.9	Shearing with recentering.	60
5.1	Stereogram master printer geometry.	63
5.2	Locations of red, green and blue separations on H1.	67
5.3	Holographic transfer printer geometry.	68
5.4	Reconstruction of the hologram.	70
6.1	CT head scan data set.	72
6.2	Histogram plot of CT head data set.	73
6.3	Computer graphically reconstructed images of child's skull.	76
6.4	Hologram of child's skull.	77
6.5	Histogram plot of MRI heart data set.	78

6.6 Computer graphically reconstructed images of opaque heart. . . . 81
6.7 Hologram of long-axis section of a beef heart. 83
6.8 Computer graphically reconstructed images of transparent heart. . 86
6.9 Test volume. 87
6.10 3D averaging filter. 89

Acknowledgments

I would like to express great thanks to Stephen Benton for offering the opportunity to work on this thesis topic, and for his guidance and support all along the way. Also, to Tom Sullivan for being the best friend I could ever have, for the moral support, the patience and the fun, more thanks than I can ever express. Many thanks to members of the MIT Spatial Imaging Group for useful discussion, and for being great work associates and friends. Thanks to Mike Halle for being a hard-working and helpful partner in this research.

This work was funded by a joint IBM/MIT agreement dated June 1, 1985.

Chapter 1: Introduction

Modern medical imaging methods such as Computed Tomography, Medical Resonance Imaging, and Positron Emission Tomography produce arrays of images of parallel cross-sections comprising a volume. The resulting slices provide a visual map of some structural or functional information inside the volume.

Two factors are fostering the development of three-dimensional (3D) display of such data. First, the continuing improvement in imaging equipment for medical scanning provides data with higher spatial resolution and increasing signal to noise ratio. Such data lend themselves well to image enhancement and computer-graphic 3D reconstruction algorithms. Secondly, as display technologies improve, different methods are becoming available for displaying these three-dimensional medical data for more complete understanding. Various methods of 3D display are available, such as the varifocal mirror, head-tracked 3D display workstations, and holographic stereograms.

The goal of this work is to demonstrate that 3D perception of spatial display of medical images can allow rapid and accurate comprehension of complex volumetric data. However,

because the vast amount of information contained within the data set may overwhelm even the extended perceptual capacity of a good 3D display system, specialized image editing and enhancement tools must evolve concurrently to maintain a clear presentation of important structures within the data.

As a result, many techniques for detecting, rendering and displaying boundaries between regions of the data volumes as surfaces have been developed, and specialized hardware to minimize image generation time have evolved. These techniques attempt to successfully convey the 3D nature of the data with the aid of visual cues available in conventional computer graphic imagery, including light and shadow, texture, perspective, color and stereopsis.

Recently, a superior algorithm for visualizing three-dimensional surfaces called *Volume Rendering* has been developed. Its results supersede those of previously developed techniques for rendering volumetric data. The algorithm renders tissue boundaries as surfaces, but avoids making any binary classification decisions in the process. As a result, the images it creates provide clear visualization of surfaces, and remain free of the types of rendering artifacts characteristic of many other 3D reconstruction algorithms. With volume rendering, a clinician can display enhanced structures of interest while attenuating tissues of less importance. Such a tool for reconstructing medical data permits the generation of images in which 3D structures of interest are clearly understandable and unobscured by less important structural or functional information.

3D editing and rendering combined with spatial display offer clinicians the opportunity to view complex spatial data in three dimensions. Since holographic stereograms provide the highest level of image quality among any of the 3D display modalities currently available to medical imaging, the choice of this method of display for images generated by a volume rendering system would provide the best spatial display for complex 3D scenes. In such a format, the entirety of information contained in many rendered perspective views of the volume is manageable and easily comprehended in one display.

Displays with such extended perceptual capacity that offer immediate and vivid insight could be advantageous in many clinical applications. For instance, by offering a more accurate presentation of bone surface orientations in three-dimensional space, holographic display can be used to plan orthopaedic reconstructive surgery. Osteotomy surgery may be enhanced if a surgeon is offered better pre-surgical visualization of the reconstruction that is necessary. Acetabular structure can be displayed optimally in a spatial format so that fracture and dislocation of the hip are clearly visible. Components of fracture of the posterior column, the medial wall, and the sacrum can also be vividly depicted. By viewing volumetric data displayed as three-dimensional surfaces, cardiologists may be able to better identify congenital defects of the heart and the great vessels. In addition, the complex vascular structure depicted by coronary and cerebral angiography can be perceived clearly and unambiguously in one spatial display.

Holographic stereograms of medical data blend the two technologies of computer

graphics and holography. Due to the availability of specialized hardware and software, computer graphic reconstruction of data is becoming more widely used by clinicians to visualize areas of interest within a volume of data. In contrast, the use of holographic stereograms in medicine is far from widespread, although such an idea is not new. It was hypothesized that the combination of volume rendering and holographic display would result in a spatial representation of medical data offering high image quality and enough added information to stimulate interest among the medical community.

In this work, an exploration of holographic display of computer-graphically reconstructed medical data is documented. The implementation of a volumetric rendering algorithm that generates computer graphic images, and the method of recording these images holographically, is also documented. Results are presented for three computer graphic sequences rendered and two holograms generated.

Chapter 2: Background

A volume of medical data consists of many planes that are usually images of cross sections through a subject. To make the information contained in this data fully comprehensible, several stages of evaluation may be necessary. First, there is a need for the ability to preview the raw image data yielded by the scans. Conventionally, volumetric data is displayed in two dimensions by a clinician, slice by slice, on a display workstation that offers interactive windowing and leveling facilities. These contrast enhancements map each data value to a new data value so that some structural or functional detail becomes more clearly visible. However, such 2D image processing algorithms by themselves may not be adequate to depict three-dimensional structure.

Secondly, as a partial remedy for this situation, a clinician may find that the ability to further interact with the data is useful. It is often desirable to filter out all but some specific structural or functional region of the anatomical data, and then view the selected tissues in a volume from a variety of perspectives. Suitable 3D image editing, processing, and reconstruction algorithms are often provided by a computer-graphic workstation with hardware tailored to these tasks. It is essential that the interface between clinician and

workstation provides the user with the ability to easily interact with the system. One would also require that image generation times not exceed a few seconds.

Lastly, there is need for a practical means of hardcopy display of the data. A collection of slices is usually presented as an array of separate two-dimensional grayscale images on a larger piece of film. These pieces of film are clipped to view boxes for small audiences of clinicians to review. Ideally, hardcopy display would be quickly and inexpensively produced, could easily be viewed and evaluated, and then filed with other relevant patient data. Such a display must clearly convey all pertinent information to a viewer so that clinical assessments can be made rapidly and accurately. A hardcopy spatial image would display the slices as spatially aligned, and could clearly depict surfaces spanning multiple slices.

2.1 Conventional 2D Display of Medical Data

2.1.1 Black and White Display Issues

When displaying medical data on an electronic display with a grayscale colormap, one could choose to present a black figure on white ground, or the reverse. Perceptual differences between white-on-black versus black-on-white displays are not well understood. Since radiologists are trained to examine radiographic film images in which tissues of the smallest electron density are imaged as the highest film density, and dense tissue appears more luminous, this convention may be the most intuitive for all grayscale display. Because

electronic imaging devices can offer either representation, a more clear understanding of the perceptual differences between images displayed both ways would be helpful.

In absence of those perceptual criteria, other image-dependent factors might be used to decide which format to favor. When either of these formats is presented on any type of luminous display, large bright luminous areas in the display may be undesirable. Flooding of the retinas by light from these areas due to intra-ocular scattering can decrease the ability to detect subtle changes in contrast in the dense portions of the image. If discrimination of these subtle changes in density are important to the evaluation of the image, it may be wise to modify the colormap so that the large luminous areas are displayed as dark areas instead. Not only does this veiling glare occur in film transparencies clipped to a view box, but it is also evident in raster displays and holographic stereograms.

Unfortunately, the wide dynamic range offered by radiographic film is unavailable in many other forms of display. For this reason, the human visual system's ability to discriminate between levels of brightness is an important consideration in the design of display equipment.

The number of brightness levels that the eye can perceive is dependent on many factors; among them are the complexity of a scene and the structure and nature of the edges within the scene. Sharp edge boundaries between two levels of brightness can stimulate a perceptual over-emphasis of the edge known as Mach banding. In addition, the gradient at the edge of an object of given contrast can have an effect on the detectability

of the object. Furthermore, contrast perceptions can occur even in the absence of either edges or luminosity changes (Cornsweet, 1970).

It has been determined that the contrast sensitivity of the human visual system peaks when a spatial frequency of about three to six cycles per degree visual angle is used as stimulus. This range of relatively low spatial frequencies seems to be most significantly considered in a person's pattern recognition process. If a display is capable of resolving more than six to eight cycles per millimeter, the ability to optically magnify portions of a displayed image may improve comprehension in the diagnostic process.

When deciding how many bits of grayscale to incorporate into an electronic display, a designer must consider these perceptual issues. Even when eight bits of grayscale are used, which provides enough brightness levels to exceed discrimination requirements of human perception, the actual display performance will largely depend on image characteristics.

2.1.2 Color Display Issues

On perceptual grounds, the use of color coding of Computed Tomogram (CT) images can be justified. While using grayscale to encode this information limits the number of perceptible brightness levels to approximately 10^3 , the number of distinguishable colors is estimated at upward of 10^6 . This display range is much better matched to the extensive information content of a complex CT slice.

However, reactions to the use of color to encode the spatial extent of anatomical structure have been unfavorable among the radiological community. Radiologists are carefully trained to comprehend the spatial map of anatomy provided by the attenuation of x-rays, and feel that the use of color to code spatial extent is superfluous, or even distracting. Indeed, the additional task of decoding the color assignment in an image, in the absence of such a standard, might add more confusion to the display in many cases. In a complex image, sharp boundaries between colors may create disturbing color contours that are confusing to a viewer. Nevertheless, in an image that contains more smoothly varying intensity throughout, color may enhance a clinician's ability to detect gradual changes in signal intensity. Color can also be used effectively and acceptably to set aside graphic and textual annotations on medical images (McShan and Glickman, 1987).

Unlike CT, which provides structural information, Positron Emission Tomography (PET) provides a study of metabolic processes by mapping the distribution of positron-emitting radioactive tracer material throughout the patient to data values. In this case, color can be used to illustrate functional assessments of metabolic processes. Since it is often desirable to detect gradual changes of signal intensity in PET, color coding can provide an effective display.

Magnetic Resonance Imaging (MRI) allows the clinician to deduce chemical composition as well as structural information. For MRI, as for CT, color is not favored by radiologists in the coding of structural information. However, color-coded display of MRI

data may be useful in some types of compositional or functional assessment.

Another way that pseudocolor techniques can be applied to MRI is derived from the processing methods for LANDSAT imagery developed by NASA (Vannier et al., 1987). Multispectral analysis and classification techniques performed on LANDSAT data can be extended to operate on MRI data. A set of MRI volumes of the same subject created by varying some imaging parameters constitutes a multispectral data set. Using this technique, color composite images of anatomical slices, and theme maps can be generated.

Because MRI data is multidimensional, it may be easier in some cases to analyze with colorization of component parts. In addition, when classification of tissue is necessary, the use of multiple volumes generated by varying imaging parameters can greatly decrease the probability of error in the classification.

2.2 Methods of 3D Editing and Reconstruction of Medical Data

Most of the techniques previously developed for 3D reconstruction of slice data can be classified as one of two types of algorithms. In the geometric approach, data is segmented into regions of interest, and geometric primitives that fit to these regions describe a surface. The other approach considers volume elements (voxels) as luminous points in a volume, and displays them as such.

2.2.1 Geometric Rendering Approach

In the geometric approach, pattern classification techniques are employed in the segmentation of the data. A general outline that fits many of these 3D reconstruction algorithms is as follows:

- object identification
- object representation / formation
- rendering of surfaces
- display of computed images

As stated above, the object identification step involves the use of a classification procedure. First, the entire volume must be segmented into regions. Then, using some *a priori* information about the object being detected, the regions that constitute the object can be identified in each slice. In the absence of *a priori* information, criteria based on the distribution of pixel values can be used for discrimination.

A general algorithm for region segmentation is stated as follows: For a volume, V , of data, comprised of a set of slices, define

$$S_k = \{v \mid 1 \leq x \leq X, 1 \leq y \leq Y, z=k\}$$

as the k^{th} slice of V . The first step is to determine a subset O of volume elements (voxels) in S as an object in V . Usually the data set is processed slice-by-slice, and the algorithm proceeds by deciding which voxels in each slice belong to the region that defines the object.

For S_k , for every k , a voxel v , is assigned to the region of interest if a certain condition $P(d(t))$ applies. t is a feature vector associated with the voxel, and $d(t)$ is a discriminant function used to classify the voxel. Selecting an optimal feature vector and an appropriate discriminant function are themselves non-trivial tasks. A good feature set may be determined on the basis of statistical analysis of the image slices. In the case of CT, for example, a mapping from the set of voxel values to a set of tissue densities, or the gradient of this mapping may be used as feature vectors.

Next a classification decision is made that matches the voxel to a region. In many cases, a set of features does not definitively classify a voxel, and statistical decision theories must be employed.

In CT, the simple case of separating bone from all other tissue, region segmentation may be achieved by a thresholding operation. Then, the discriminating criterion is given by

$$P(d(t)) \in R$$

where t is a CT number representing a density value used as the feature set, and R is a range of density values. Resulting from the segmentation in each plane is a set of voxels, O_k ,

$$O_k = \{v \mid v \in S_k, P(d(t))\}$$

where O_k defines a connected set of voxels to be the object of interest, O . Once the regions of connected voxels constituting O are known, it remains to develop information about the contours of these regions. The use of contours to characterize an object in a scene involves an algorithm that can be broken down into several steps. First, all edge elements in a scene must be detected. Secondly, the edges must be assembled together to form contour lines, and finally these contour lines must be grouped to be part of some structure.

There are many different methods of contour detection and object representation. In general, descriptions of contours bounding the regions of interest are generated for every slice in the volume. 8-contours (Herman and Udupa, 1983) store and allow fast access to information about the borders and the internal structure of an object. This feature facilitates quick manipulation of the surfaces in three space. The chain-code representation (Heffernan and Robb, 1985) of a contour can be nicely smoothed, helping to alleviate jagged surfaces that owe to the cubic structure of the voxels from which they were defined. And the Fuchs-Kedem-Uselton method (Fuchs et al., 1977) computes a surface of minimum area by minimizing a path through a graph. This algorithm yields a

smoothed surface that is piecewise polygonal. The marching cubes algorithm can produce superb surface detail, and can be extended to include texture mapping and transparency (Lorensen and Cline, 1987).

2.2.2 Luminous Voxel Method

In the second category of 3D reconstruction methods, voxels are considered as luminous points arranged in a volume with degrees of luminance corresponding to their voxel values. An integration along the line of sight through the volume is usually performed for each pixel in the image, and yields a final image that looks quite like a radiograph. Voxel values that correspond to uninteresting tissue types can be ignored by a more intelligent integration method, so that an image showing only tissues of primary interest can be created (Kulick et al., 1988).

This type of algorithm considers *all* voxels in its visibility calculation, as opposed to the previously mentioned class of algorithms that decides which voxels constitute a surface in its segmentation and classification steps. However, luminous voxels convey little information about the tissue boundaries. For example, no occlusion cues are available to the viewer. Ideally, a reconstruction algorithm would convey as much information about the structure of tissue surfaces as was available in the data set, and would avoid making binary classification decisions that may result in unwanted rendering artifacts. Such artifacts stemming from misclassified tissue may manifest themselves as randomly appear-

ing surfaces or holes in tissue boundaries, and degrade the integrity of the reconstructed images.

2.2.3 Volume Rendering

Recently, research toward better reconstruction methods has resulted in the *volume rendering* approach (Drebin et al., 1988, Hohné and Bernstein, 1986, Levoy, 1988). This volume rendering method bypasses the need for surface detection altogether, and employs every voxel in its visualization calculations. The strength of this algorithm lies in its avoidance of classification decisions. The volume rendering algorithm employs the use of calculated gray level gradients which dual as surface normals allowing the rendering of surface information with extraordinary detail. Because the method never has to decide whether or not a surface passes through a particular voxel, it avoids generating spurious surfaces, or creating holes in places where there should be none. By avoiding both surface detection and surface geometric representation, a more direct volume visualization is realized. As a result, a reliable representation of the information in the raw scan volume is available along with the ability to emphasize structures of interest within the volume, and de-emphasize those of less importance.

2.3 2D Display Shortcomings

Even the superior images generated with the volume rendering technique cannot completely convey the details about the dimensionality of the data to the viewer. Despite clever use of monocular cues to depth in the image, the orientation of surfaces and their location relative to one another in space remain ambiguous. However, depth information can be conveyed by 2D displays by exploiting the kinetic depth effect. By displaying a sequence of frames of a rotating scene, motion parallax is provided and a perception of kinetic depth is achieved. Studies comparing motion parallax and stereopsis have found that both mechanisms provide similar comprehension of three dimensional textured surfaces (Rogers and Graham, 1982). However, whenever the rotation is interrupted to facilitate a closer inspection of the volume from one perspective, the depth information is again unavailable to the viewer. The obvious advantage offered by “true” three-dimensional display are their ability to clearly present spatial data in spatial form.

2.4 Role of Three-Dimensional Display in Medical Imaging

2.4.1 Cues to Depth

A variety of perceptual cues trigger physiological and psychological mechanisms to provide a viewer with a sense of depth in a scene. Both monocular and binocular kinds of cues

work together for the perception of depth (Okoshi, 1976).

Monocular cues to depth perception hinge on the experience and imagination of the viewer evaluating a 2D projection of a 3D scene. Some of the cues are: occlusion, light and shadow, relative size, linear perspective, aerial perspective, texture gradient, color and monocular motion parallax. Effective two dimensional display of spatial data relies on the exploitation of these cues for the ability of a viewer to interpret the depth of a scene with reasonable reliability.

However, the most reliable and compelling impressions of depth arise from the presentation of different perspectives to the two eyes, and the presentation of perspectives that vary with viewer location. "True" three-dimensional displays use these techniques to take full advantage of our perceptual capacity to interpret distances between objects and orientations of surfaces. The viewer can use both the physiological cues to depth and the psychological ones. The physiological cues include accommodation, convergence and binocular parallax. Even in a simple stereo pair display, though motion parallax and possibly other monocular cues are absent, the binocular cues available can add significantly to the comprehension of the locations and orientations of objects in the scene.

2.4.2 Slice Stacking

Various techniques for displaying stereo pairs of data have been devised, including wavelength multiplexed, and temporally multiplexed displays, and stereo slide viewers. Although these devices have been available for a long time, their lack of popularity may be attributed, at least in part, to the required use of viewing aids such as colored spectacles or specialized optical viewers.

Autostereoscopic displays do not impose such limitations on the viewer. One such form of true 3D display that has been discussed in the literature is that of the varifocal mirror display. This technology displays a stack of optically superimposed slices and is well suited for operator-interactive visualization of the data in three-dimensions. However, the varifocal can only display a limited number of voxels. In addition, the resulting 3D image will not contain any occlusion of tissue from overlapping structures, and thus a powerful cue to depth is unavailable in this form of spatial display. Furthermore, conventional two-dimensional recording methods cannot capture in hardcopy form the depth dimension inherent to the varifocal mirror's display.

2.4.3 Holographic Display of Medical Data

Holographic stereograms afford the useful ability to use computer-graphic images as component views. These views can be enhanced to contain many cues to depth. Thus

medical computer-generated holographic stereograms combine the best features of computer graphics and spatial display, and can provide an excellent visualization of a volume of data.

Holography was first developed by Dennis Gabor in 1947 while he was working to improve the resolving capabilities of the electron microscope. In 1962, the first practical off-axis holograms were made by Emmett Leith and Juris Upatneiks. This development of off-axis holography in combination with R. V. Pole's work in 1967 on synthetic holography paved the way for high-quality holographic stereography.

The use of holographic stereogram techniques as a means of displaying medical images taken from multiple viewpoints is not new. The recording of integral holograms using radiographic information is a well-established idea (Benton, 1973, Hoppenstein, 1973). Sequences of x-ray photographs of different perspectives are generated by moving the cathode ray source and the camera unit, mounted on a U-arm, that records the x-ray image of the patient. However, in many cases, the number of perspective images acquired is minimized to reduce patient exposure and the resulting holograms have a narrow field of view. Some computer-based x-ray systems employ backprojection algorithms to interpolate intermediate frames between the acquired ones, and thus permit the set of images to include many more perspective views. Although such displays are not considered as being of clinical value yet, many experimental holograms have been generated using sequences of x-ray photographs (Lacey, 1987, Tsujiuchi et al., 1985).

Holographic stereograms in many formats have also been created using sequences of images reconstructed from volumetric data (Benton, 1987, Fujioka et al., 1988). The success of the holographic image relies heavily on the quality of the component images used to produce the stereogram, as well as on the limitation of distortion and artifacts introduced by the holographic process. To date, holographic display of volumetric medical data has relied upon both geometric methods and luminous voxel methods to reconstruct a medical scene from multiple viewpoints. With the application of volume rendering to the holographic pipeline, the resulting spatial image can depict more exactly the information of interest contained within the acquired volume. The integrity of the surface visualization can allow clinicians to trust the reconstructed image as an accurate representation of the acquired data. Furthermore, the increased perceptual potential of the display can manage these complex dimensional data in an exceptionally intelligible manner.

Chapter 3: Volume Rendering Analysis

A volume renderer makes use of the entire volume of data in its reconstruction of the surfaces contained within. Several additional volumes of information are computed and stored during the rendering process.

The slices of data containing tissue electron or proton density values at every voxel are kept available for the renderer to access during the rendering process. From this data volume, a volume of density gradient vectors is computed. These gradient vectors are used to approximate the surface normal at every voxel in the illumination calculation.

In addition, every voxel is assigned a degree of opacity. These opacity values (with zero opacity corresponding to a completely transparent tissue) are stored in an opacity volume. The mapping between data density values and the opacity of voxels that is used to compute the opacity volume is user-specified, and permits interactive emphasis on tissues of interest.

A volume containing color information for every voxel is also computed. The RGB color components at a voxel are derived from an illumination calculation which models

the reflection of light from the surface specified at the voxel back to the eyepoint. If color-coding information for tissue types is not included in the algorithm, the light source color can be used to determine the color at a voxel location.

A ray tracing process is used to cast rays from every image pixel through the volume of voxels. The color and coverage (transparency) of each image pixel are determined from color and opacity contributions of voxels along a viewing ray cast from that pixel.

In the following sections, the acquisition of medical data as well as the calculation of voxel grayscale gradients, opacities and colors will be outlined in greater detail.

3.1 Medical Data Acquisition

The volume rendering algorithm examined here relies on digital data for computer graphic 3D reconstruction. As a result, only medical imaging techniques that provide an electronic stream of data (such as computed tomography, and magnetic resonance imaging) have been considered as sources of medical images.

Computed tomography is the most common computer-based medical imaging technique. CT employs the use of many projection radiographic images which can be used to reconstruct the three-dimensional anatomical information. Because various tissue types possess different electron densities, x-rays from a cathode ray source that pass through a series of tissues are attenuated according to the density of each. An array of sensors

opposite the source detects radiation corresponding to a distribution of electron densities along a set of paths. One method for reconstruction, known as back projection, uses the output of each sensor group to produce a two dimensional image of tissue density convolved with the point spread function of the sensor. Deconvolution with the known point spread function yields the set of slices in the form in which they are viewed and evaluated. These slices also serve as input to the three-dimensional computer graphic reconstruction algorithm.

CT provides both good spatial resolution (Figure 3.1) and high signal to noise ratio of the data. Specifications on these parameters were obtained for an typical CT scanner, and are provided in the figure.

Rather than illustrating the structural nature of the anatomy as CT does, MRI primarily provides a description of the chemical composition of the subject. The generated images record the manner in which the chemical constitution of a particular tissue type behaved during the scan. In the presence of a large static magnetic field, the magnetic moment of protons within the tissue align with the field. When a field perpendicular to the static field is introduced as a perturbation, the magnetic moments of the protons precess about the axis of alignment. This precession oscillation is detected with a radio-frequency (RF) coil.

The most prominent contributor to the oscillation is the proton, (H^+), which facilitates imaging of soft tissue superior to that of CT. MRI also allows the assessment of the

CT	spatial resolution	(high res)
	0.75 mm	0.45 mm
MRI	spatial resolution	SNR
	3 mm	head coil 60
		body coil 80

Figure 3.1: Average CT and MRI specs, courtesy General Electric Inc.

magnetic susceptibility of a region which can indicate blood pools. In addition, the availability of phase information in the MRI data permits blood flow evaluation.

After any number of possible MRI experiments that produce frequency data, a two- or three-dimensional Fourier transformation yields the spatial map of tissue composition. In this final form, the data can be viewed slice by slice or can be used as input to a 3D reconstruction algorithm. MRI, like CT, provides good spatial resolution, although the signal to noise ratio (SNR) is often inferior to that of CT (Figure 3.1).

For our purposes, data having high spatial resolution is of great importance, and for this reason the imaging modalities considered in this work exclude PET, SPECT, and many others. MRI and especially CT, however, provide excellent volume data sets for the 3D reconstruction algorithm explored in this thesis.

3.2 Gradients as Surface Normals

The volume rendering method of 3D reconstruction uses every voxel in the volume to generate a computer graphic medical image. In order to render all points inside a volume, a method of illumination calculation is necessary. Modeling the manner in which light behaves on a surface requires knowledge about the surface's orientation. Volume rendering makes use of the fact that surface normals can be approximated by the grayscale gradients of the slice data. At interfaces between different tissue types, the gradient magnitude

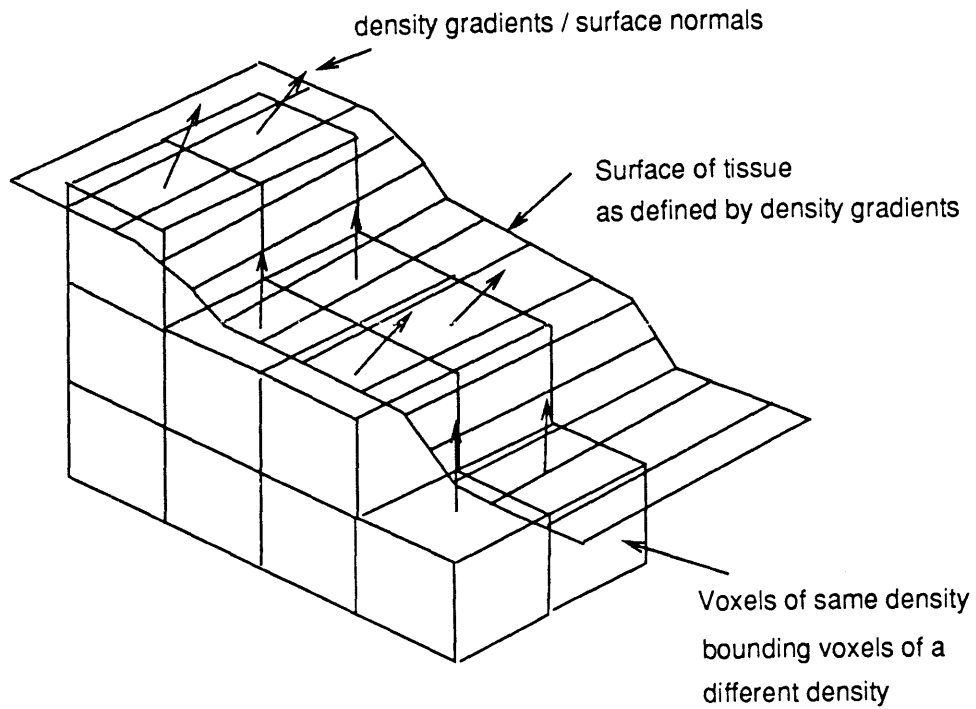


Figure 3.2: Gray-level gradients as surface normals.

indicates the surface *priority*, and the components of the vector specify the orientation of the surface at that point in the volume (Figure 3.2).

The gradients are given by

$$\nabla d_1(\mathbf{x}) = \left\{ \begin{aligned} &1/2 [d(x_{i+1}, y_j, z_k) - d(x_{i-1}, y_j, z_k)] \hat{i}, \\ &1/2 [d(x_i, y_{j+1}, z_k) - d(x_i, y_{j-1}, z_k)] \hat{j}, \\ &1/2 [d(x_i, y_j, z_{k+1}) - d(x_i, y_j, z_{k-1})] \hat{k} \end{aligned} \right\}$$

where $d_1(\mathbf{x})$ is the voxel value at point $\mathbf{x} = (x_i, y_j, z_k)$ in the volume, and represents

either tissue density in the case of CT, or the proton density of tissue in MRI.

Since spatial resolution is not infinite, however, interplane sample points in the data volume may not adequately represent small tissue neighborhoods. With this point in mind, an approximation to the gradient can be made which may work better on the sampled data.

$$\nabla d_1(\mathbf{x}) \simeq \left\{ \begin{aligned} & [d(x_{i+1}, y_j, z_k) - d(x_i, y_j, z_k)] \hat{i}, \\ & [d(x_i, y_{j+1}, z_k) - d(x_i, y_j, z_k)] \hat{j}, \\ & [d(x_i, y_j, z_{k+1}) - d(x_i, y_j, z_k)] \hat{k} \end{aligned} \right\}$$

This approximation can be used if the data has been processed to reduce any noise introduced in the acquisition process. Spurious gradient vectors produced by noisy data may indicate surfaces where none should be found. A simple averaging filter passed over the slice data can help remove high frequency noise and improve the integrity of the gradient calculation.

3.3 Grayscale to Opacity Mapping

In order to construct a useful mapping between voxel data values and voxel opacities, some assumptions must be made. To illustrate these assumptions, it is useful to consider the histogram plot of the voxel data. An idealized histogram plot of a CT volume is shown

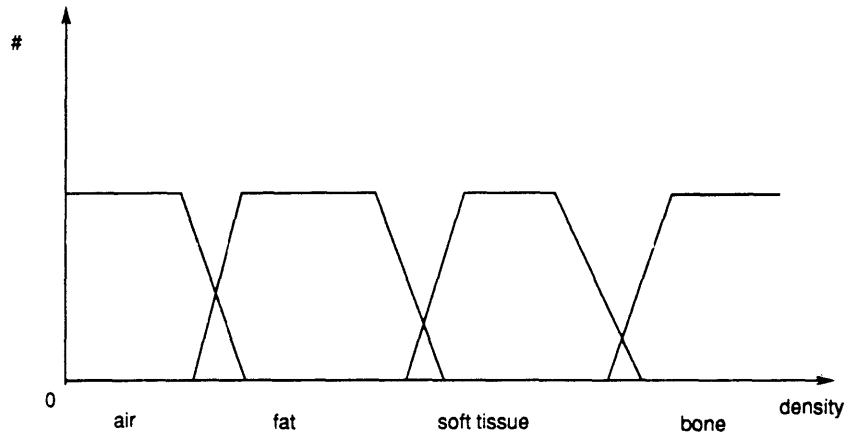


Figure 3.3: Idealized histogram plot of CT volume.

in Figure 3.3.

Using CT numbers ordered from the smallest to the largest value, assuming that each tissue touches only the types adjacent to it in the ordering, and in addition requiring that each tissue type touch at most two other tissue types, we can construct a piecewise linear mapping from voxel values $d(\mathbf{x})$ to opacity values $\alpha(\mathbf{x})$.

CT data is made up of arrays of voxels whose byte values specify the radio-opacity of tissue at each sample point. The fact that three major tissue types (fat, soft tissue, and bone) attenuate the source radiation distinctively is a great advantage, facilitating easy classification of tissue in most cases.

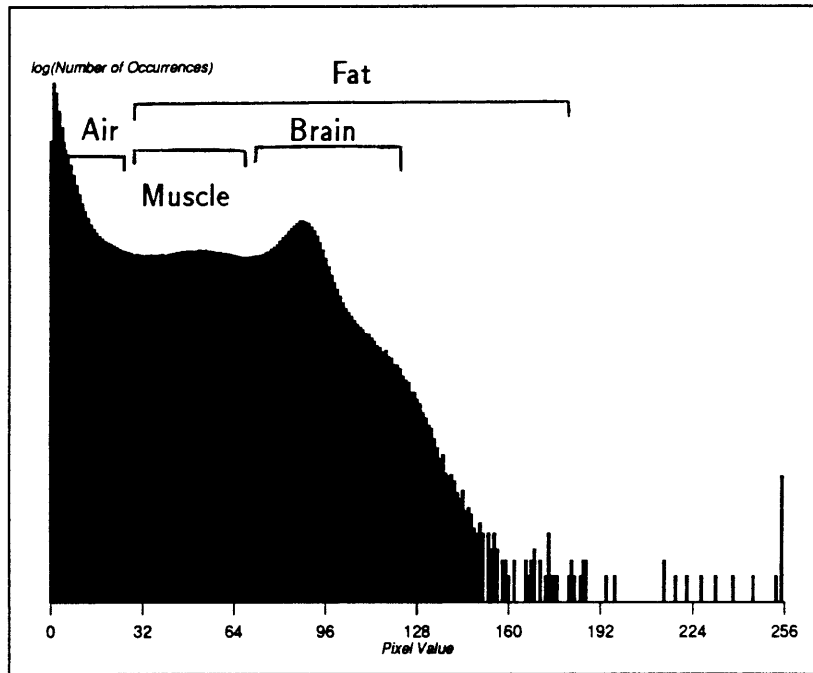


Figure 3.4: Histogram plot of MRI volume.

Because MRI reflects the chemical composition rather than structural extent of the subject, no satisfactory method has been found to use the voxel values to classify tissue type unambiguously. The fact that different tissues may have similar composition results in their representative data values having overlapping distributions. A histogram of an example MRI head scan (Figure 3.4) illustrates the manner in which MRI data violates the assumptions mentioned above that govern the grayscale to opacity mapping. As the histogram shows, successful discrimination can be made between ambient noise and tissue, and an air tissue interface is also usually obvious. As a result, only MRI experiments that result in the imaging of *few* tissue types have successfully been rendered in this work.

3.4 Opacity Calculations

In order to provide a user with the ability to separate a structure of interest from surrounding tissues, less interesting tissues can be assigned a high degree of transparency. With the ability to interactively assign opacities to selected tissue densities, a user can look through the volume, viewing opaque structures of interest surrounded by transparent ones of secondary importance.

In a user-specified grayscale to opacity mapping, a user can assign specific opacity values to grayscale values. The grayscale value at a particular voxel location is either numerically bounded between two grayscale values specified in the mapping or is simply equal to one of the specified values. An opacity at that voxel location is then found by linearly interpolating between the two opacity values corresponding to two grayscale values specified in the mapping.

Since, however, the focus of this thesis is on visualizing *surfaces* that clearly present the 3D shape of many anatomical features, suppression of interior tissue visibility and enhancement of tissue boundaries is desired. This visualization is achieved by using the density gradient as a scale factor in the opacity calculation. The expression used for opacity computation is as shown below.

$$\alpha(\mathbf{x}) = \begin{cases} |\nabla d(\mathbf{x})| \left\{ \alpha_{v_{n+1}} \left\{ \frac{d(\mathbf{x}) - d_{v_n}}{d_{v_{n+1}} - d_{v_n}} \right\} + \alpha_{v_n} \left\{ \frac{d_{v_{n+1}} - d(\mathbf{x})}{d_{v_{n+1}} - d_{v_n}} \right\} \right\} & \text{if } d_{v_n} \leq d(\mathbf{x}) \leq d_{v_{n+1}} \\ 0 & \text{otherwise} \end{cases}$$

where $d(\mathbf{x})$ is the density at the sample voxel location, d_{v_n} and $d_{v_{n+1}}$ are the lower and upper-bound densities, and α_{v_n} and $\alpha_{v_{n+1}}$ are the lower and upper-bound opacities, specified in the mapping. $|\nabla d_1(\mathbf{x})|$ is the magnitude of the density gradient at the sample voxel location. It is clear from this formula that when a voxel is surrounded by voxels of the same tissue density, then its corresponding density gradient will be zero, yielding a zero-valued opacity as well. This design allows us to visualize the boundaries between tissues, and to ignore tissue interiors.

3.5 Color Calculations

A number of methods for shading the anatomical surfaces are available (Foley & Van Dam, 1984). The simplest shading model is the depth-color display. This codes the voxel brightness as a function of its distance from the viewer. If hidden surface removal is applied to the data set concurrent with this shading approach, an effective display of three-dimensional data can be achieved. Alternatively, even more sophisticated lighting

models can be applied in the calculation of voxel color. By modeling the surface as a Lambertian one, the illumination calculation at a voxel depends both on the surface orientation and the eye position. Especially in the case of direct volume visualization, it is useful to also include the intensity of specularly reflected light. This addition to the illumination model can highlight the more intricate surface modulations.

The Fresnel equation governs the directional behavior of specularly reflected light. For imperfect reflecting surfaces (those that are not mirrors) the amount of light received by the eye depends upon the spatial distribution of the specularly reflected light. Smooth surfaces reflect light with a narrow spatial distribution, while reflected light from rougher surfaces is more widely spatially distributed.

Phong's empirical model for the characteristics of specularly reflected light provides a useful model for implementation. Specifically,

$$I_S = I_I w(\theta, \lambda) \cos^n \phi$$

gives the intensity of the specularly reflected light, and $w(\theta, \lambda)$ is the reflectance curve giving the ratio of the specularly reflected light to the incident light as a function of incidence angle, θ , and the wavelength, λ . I_I is the incident intensity from a point light source. The value of n is a power used to control the spatial distribution of incident light.

ϕ is the angle that the reflected ray makes with the line of sight.

The complete illumination model which combines ambient, diffuse, and specular lighting effects is stated as follows:

$$I = I_A K_A + I_i / (d+K) \{ K_D \cos\theta + w(\theta, \lambda) \cos^n \phi \}$$

I_A is the ambient light intensity, without which the surface will appear in a non-atmospheric space with no scattered light. K is an arbitrary constant and d represents the distance of the object from the viewer. K_A , K_D and K_S are coefficients of the ambience, diffuseness and specularity of the surface, respectively. This illumination calculation is performed for every voxel, using the gradient vector at that voxel location as an analog of the surface normal vector.

The calculation of color contributions to a final pixel color by the sample points along a viewing ray was extended by Levoy (Levoy, 1988) from work done by Blinn (Blinn 1982). The volume of data is modeled as a cloud of spherical particles. A single scattering cloud model is used, in which the proportion of light reflected by a particle is small (less than 0.3).

If there are n particles per unit volume, then n is called the particle number density. The proportion of the cloud volume occupied by particles of radius p is the particle number

volume multiplied by the particle volume.

$$D = n \left(\frac{4}{3}\right)\pi p^3$$

Because the overlapping of particles is not physically possible, the probabilities of particles situated inside a volume are *not* strictly statistically independent. The occurrences of several particles inside a volume can be considered independent events if it is assumed that D is small owing to low particle number density.

Under this assumption, the probability of K particles in volume V can be expressed as the Poisson process,

$$P(K;nV) = \sum_{r=0}^K \frac{(nV)^r}{r!} e^{-nV}$$

where nV is the expected number of particles in V . The probability that zero particles are contained in V is given as

$$P(0;nV) = e^{-nV}$$

and likewise, the probability that the number of particles in volume V is greater than zero is

$$P(> 0; nV) = 1 - e^{-nV}$$

Levoy develops the model for computing voxel brightness as follows. In a cylindrical sub-voxel beam of radius p passing through Z voxels, if one or more particles are encountered in voxels $z+1$ through Z (closest to eye), then the brightness of the beam is given by

$$P(> 0; nV_z, 0; nV_{z+1}, \dots, 0; nV_Z) = (1 - e^{-n_z V_z}) \prod_{m=z+1}^Z e^{-n_m V_m}$$

The resulting brightness due to contributions along a ray having the same height and width as a voxel passing through Z voxels of unit volume ($V_z=1$) is as below.

$$B = \sum_{z=0}^Z \{ B_z (1 - e^{-n_z}) \prod_{m=z+1}^Z e^{-n_m} \}$$

Substituting $\alpha_z = 1 - e^{-n_z}$, the following can be obtained:

$$B = \sum_{z=0}^Z \{B_z \alpha_z \prod_{m=z+1}^Z (1 - \alpha_m)\}$$

This representation of brightness allows computation of pixel color from color and opacity samples along a viewing ray using the following:

$$C(i,j) = \sum_{k=0}^K \{c(x_i, y_j, z_k) \alpha(x_i, y_j, z_k) \prod_{m=k+1}^K (1 - \alpha(x_i, y_j, z_m))\}$$

where K is the total number of sample points, $c(x)$ s and $\alpha(x)$ s are colors and opacities determined through bi-linear interpolation at the sample points, and an initial $c(x_i, y_j, z_0)$ is the color of the foreground with $\alpha(x_i, y_j, z_0) = 0$.

Using these models for illumination and transparency, color contributions along rays tracing from pixels in the image plane through the volume are summed from front to back, and a final rendered view is created. It should be noted, however, that the transparency model, while allowing the occlusion or attenuation of particles by one another, does not take refraction into account.

Chapter 4: Design of Volume Renderer

4.1 Overview of the Rendering Process

The input to the renderer is an array of images (Figure 4.1), created by a CT or MRI scan. Each 8-bit or 16-bit valued voxel represents a tissue electron or proton density, respectively. The raw data values $d_0(\mathbf{x})$ at voxel locations $\mathbf{x} = (x_{i_0}, y_{j_0}, z_{k_0})$ may require interpolation, most likely in the inter-plane direction to create more slices, or may require contrast enhancement or filtering.

Isotropic data (cubic voxels) will lead to undistorted reconstructed images, though acquired data is usually anisotropic. Consequently, a number of slices must be interpolated between each pair of originally acquired slices, depending on the ratio of slice-separation to in-plane pixel spacing.

$$\# \text{ interpolated slices} = \frac{(\text{slice separation} - \text{inplane pixelspacing})}{(\text{inplane pixelspacing})}$$

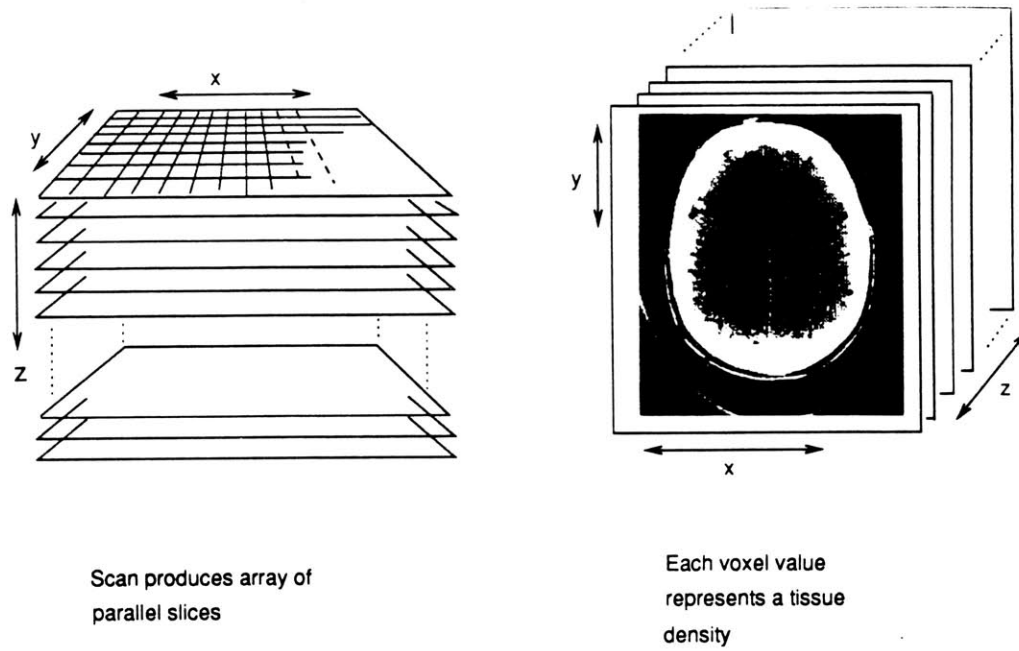


Figure 4.1: Array of slices comprising a volume.

Both intra- and inter-slice interpolation, contrast enhancement and low pass filtering to reduce noise comprise a data preprocessing step that yields a volume of prepared values, $d_1(\mathbf{x})$, at voxel locations $\mathbf{x} = (x_i, y_j, z_k)$ (Figure 4.2). The $d_1(\mathbf{x})$ are used as input to the mapping procedure which classifies grayscale values to tissue type corresponding to opacity values $\alpha(\mathbf{x})$. In addition, the $d_1(\mathbf{x})$ are used to compute gray-level gradients, $\nabla d_1(\mathbf{x})$, for all voxels in the volume. As mentioned previously, these gradient vectors will serve as surface normal vectors in the illumination calculations of the render (Figure 4.3). The gradient calculation needs to be done only once for the prepared data set.

Each time a user wishes to change the transparency of tissues in a data set, a new grayscale-to-opacity mapping must be constructed, and a corresponding opacity volume must be calculated. Both the data volume and the gradient volume are used to find the opacity volume (Figure 4.4). The gradient magnitude serves as a priority indicator of surfaces such that the surface boundaries, where gradient magnitudes are substantial, are enhanced, and tissue interiors are transparent.

Due to limited disk space, only these three volumes, data, gradients and opacities, are stored during the rendering. Once these volumes are at hand, the rendering can begin. The entire pipeline is shown in Figure 4.5. For each plane of data, the $\nabla d_1(\mathbf{x})$ are used to compute colors at every voxel location. These colors, $c_\lambda(\mathbf{x})$, are calculated by evaluating the Phong model at every point. Calculations for color are done as needed, and are not written to memory for future use.

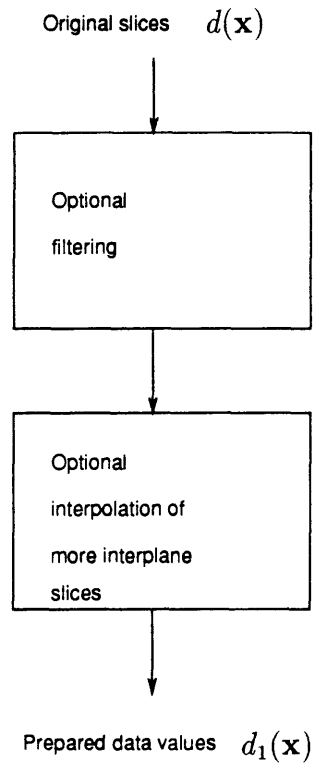


Figure 4.2: Data preprocessing step.

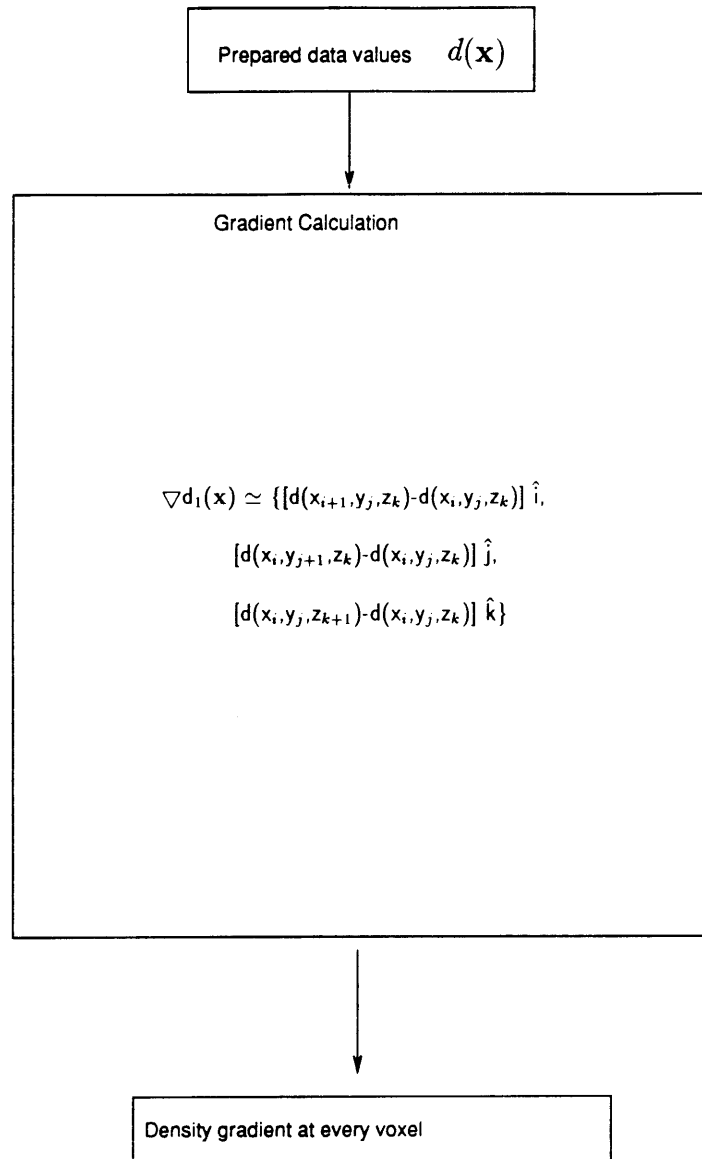


Figure 4.3: Voxel gray-level gradient calculations.

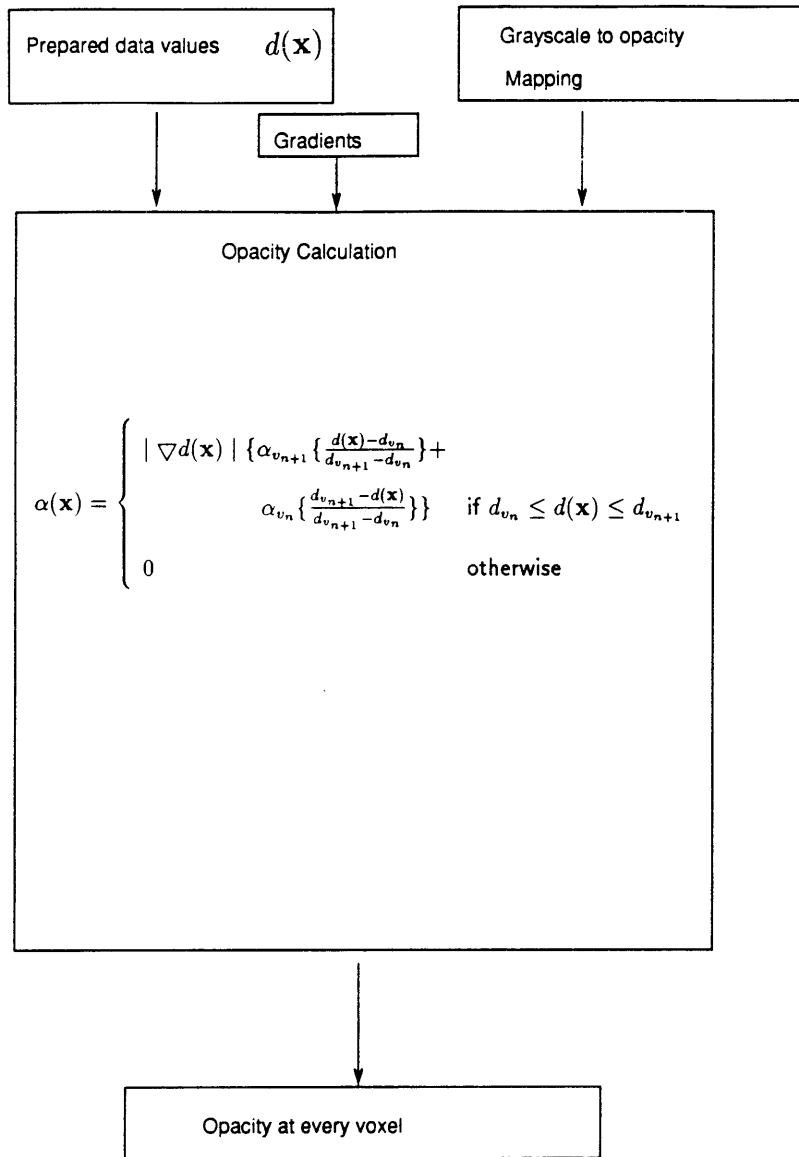


Figure 4.4: Voxel opacity calculations.

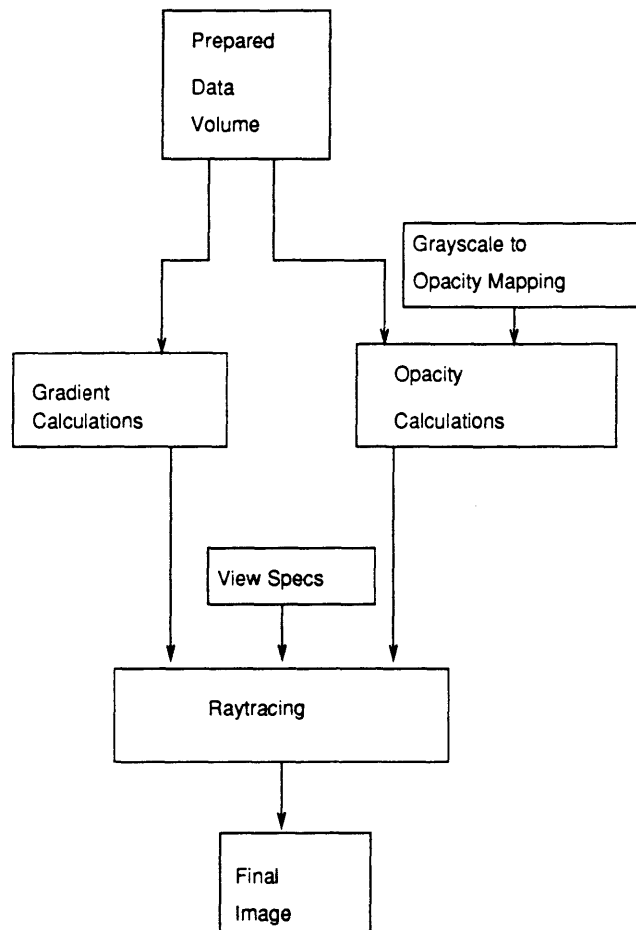


Figure 4.5: Rendering Pipeline.

Color contributions are computed for each sample point along a viewing ray by bilinearly interpolating colors and opacities in the four voxels closest to the ray intersection location in the volume. Since one ray is cast per image-plane pixel, final pixel colors are built up of color contributions from some number of evenly-spaced sample points along each ray. By casting rays through every image-plane pixel, the 3D reconstruction of the data is realized.

4.2 Ray Tracing

The ray trace algorithm is extremely parallel in nature. Ideally, it is suited for implementation on a parallel architecture, where each ray could be evaluated by a separate processor. Such an implementation would be the most efficient one.

However, the flow of the algorithm had to be reformatted to perform optimally on a Von Neumann machine, and thus the inherent parallelism has been destroyed in this implementation. Because the entire data, gradient, and opacity volumes would not fit into core memory simultaneously, design considerations were made to sequence through the volumes efficiently. These volumes are examined plane by plane, with each plane being loaded into memory only when the ray calculation requires it. As a result, the working set (the data that the algorithm is using at any one time) will be resident in fast memory for the processor to use. All other data is held on disk until needed.

For every image-plane pixel, one ray is cast. The number of evenly spaced sample points along the rays can be varied by the user. Usually, two sample locations per voxel are used to insure that every voxel is adequately represented along the ray from any viewpoint. An orthographic projection is achieved by casting rays parallel to one another. Using an orthographic rather than perspective projection greatly increases the speed of the algorithm.

Before calculating any color contributions along the rays, the ray slope must be determined. This calculation is achieved by evaluating the slope of a line from the eyepoint to the center of the data volume, usually point (0.0, 0.0, 0.0). This slope is applicable to all of the parallel viewing rays. Using the user-specified sample-point spacing, steps Δx and Δy are determined that represent the distance from one sample point to another along the x and y axes. (It should be noted that eyepoint movements are limited to horizontal variation in this implementation, a reasonable restriction for animations destined for holographic horizontal-parallax-only (HPO) display.) Pseudocode for the ray tracing loop is presented below.

- Initialize all rays in front plane of volume
- Initialize final image to have $c_\lambda(\mathbf{n}) = (0,0,0)$

for all $\mathbf{n} = (u_i, v_j)$, for $0 \leq i < \text{image width}$,

and $0 \leq j < \text{image height}$.

- Initialize coverage file to have

$$\alpha(\mathbf{n}) = 0 \text{ for all } \mathbf{n} = (u_i, v_j),$$

for $0 \leq i < \text{image}$ and $0 \leq j < \text{image height}$.

- Calculate color at every voxel in the front two planes in the volume

- For each sample point increment along the rays

{

- If sample points have moved between two *new* planes

- Calculate color at every voxel in the two planes

corresponding to data and gradient planes surrounding

the current ray sample points

- Else

- Use two previously calculated color planes

- If image-plane pixel coverage $<$ some MAX OPACITY

{

- Perform bilinear interpolation at each sample point

to find the color and opacity

- Contribute these sample points to the final image

- Update pixel coverage information in the coverage file

}

- Increment all rays by $(\Delta x, \Delta y)$ to next sample points.

}

Figure 4.6 illustrates this process. In the figure, when the new set of sample points is incremented to example plane P_1 , colors for all voxels in plane **A** and for all voxels in plane **B** are calculated. Also, previously calculated opacities for voxels in plane **A** and **B** are read into memory.

A ray structure contains the location of all the new sample points. At each sample point, the contribution to the corresponding image pixel is computed by bi-linearly interpolating color values and opacity values from the four nearest neighbors (Figure 4.7). The interpolation yielding the color at a sample point s is

$$c_\lambda(\mathbf{s}) = y((1-x)c_\lambda(\mathbf{a}_1) + xc_\lambda(\mathbf{a}_2)) + (1-y)((1-x)c_\lambda(\mathbf{b}_1) + xc_\lambda(\mathbf{b}_2))$$

and likewise opacity at s is

$$\alpha(\mathbf{s}) = y((1-x)\alpha(\mathbf{a}_1) + x\alpha(\mathbf{a}_2)) + (1-y)((1-x)\alpha(\mathbf{b}_1) + x\alpha(\mathbf{b}_2))$$

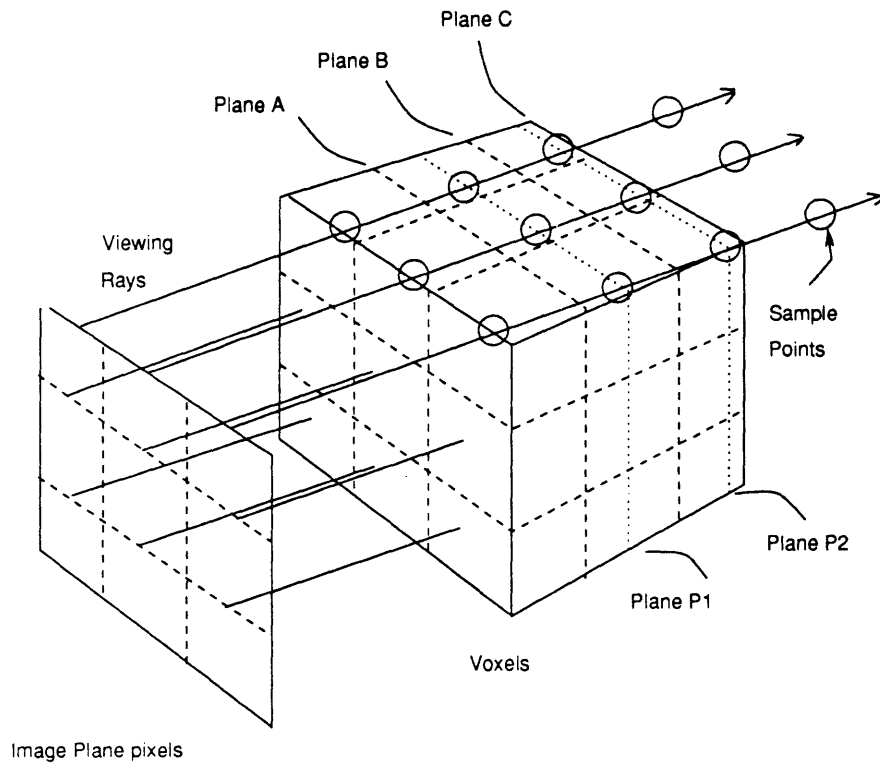


Figure 4.6: Ray tracing through the volume.

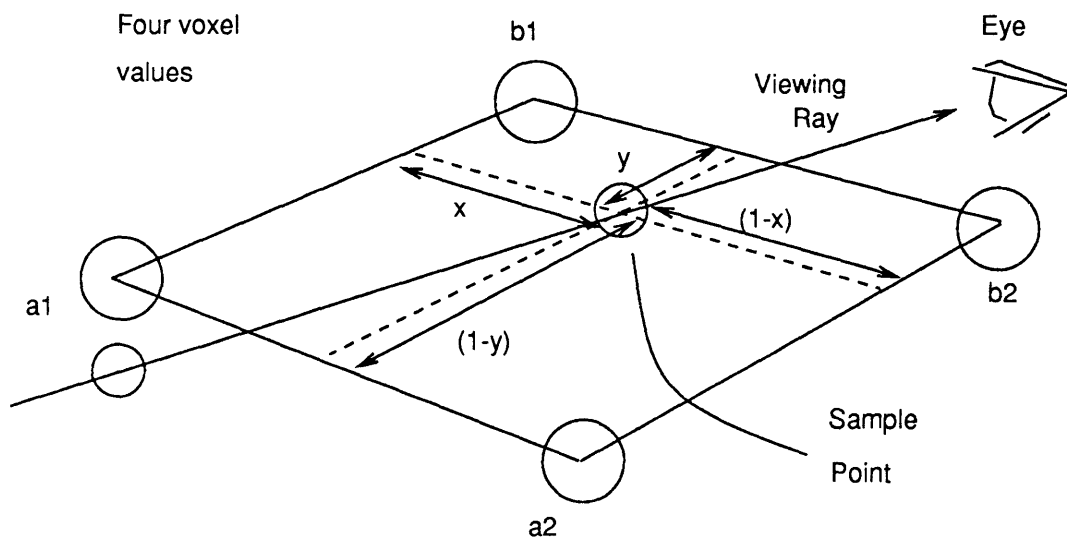


Figure 4.7: Bilinear interpolation of color and opacity values.

In addition, the information in a coverage file, which contains the opacity of every pixel and can be used to composite images together, is updated using the opacity of the new sample points.

The coverage file can be initialized to indicate zero coverage with the final image being initialized to have $c_\lambda(\mathbf{x}) = (0, 0, 0)$. Alternatively, the compositing of images can be achieved by filling the final image with another previously computed image, and initializing the coverage file with the corresponding coverage information. This type of compositing, however, would *not* accurately combine a rendered image of one tissue with that of another, if both tissues occupy the same part of the volume. Rather, a rendered image of a region of tissue entirely in *front* of another region of tissue can be composited with the rendering of that region. This technique is useful when disk space is inadequate for accommodating a large data volume. By splitting up the volume, an image can be rendered in two passes. In addition the final coverage file can be used to composite the final rendered image to some other background in a post-processing stage.

Once all sample points in plane P_1 have contributed to the final image, each point is incremented by $(\Delta x, \Delta y)$ in plane P_2 . Computed colors for voxels in plane C now replace the ones which were kept for plane A , and previously calculated opacities for plane C are written over the ones kept also for plane A .

This process repeats until all of the sample points have been considered, at which time the final image is complete.

4.3 Rendering for Holographic Display

As mentioned previously, the eyepoint in this implementation is free to move only about the equator of the data. No eyepoint movement along the vertical axis is supported, which allows interpolation in the calculation of color and opacity of sample points to be done in only two dimensions, rather than three.

It is possible to specify any viewing distance from the volume center. For single frames intended for 2D display, any view distance along a projection ray will yield the same result, since orthographic projection is used. However, since sequences of views are rendered for recording integral holograms, the view throughout the animation must imitate the hologram's view zone specifications (Figure 4.8).

The eyepoint moves along a linear track looking toward the volume from a distance equal to the final hologram viewing distance while recentering on the volume for each new view (Figure 4.9). Figure 4.9 also shows that resulting views contain no perspective foreshortening as a result of using orthographic projection. For each successive view, the eyepoint is moved a distance of the master hologram slit width (3 mm) multiplied by a horizontal magnification factor. The viewing specifications for a sequence of views for flat format holographic stereogram display are designed to fit the geometry below, using an H1 width equal to 300 millimeters, and a transfer hologram (H2) width of 254 millimeters.

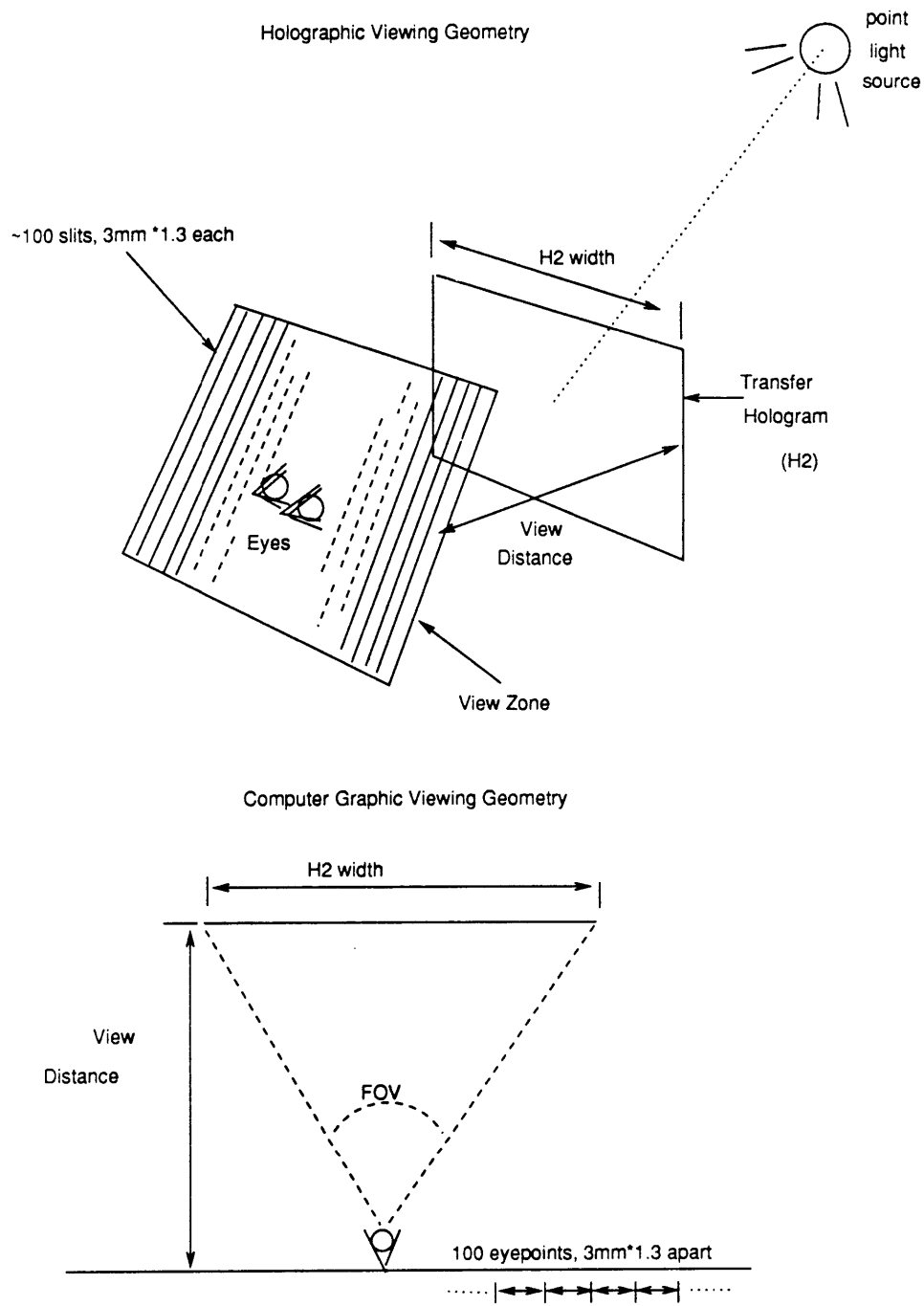
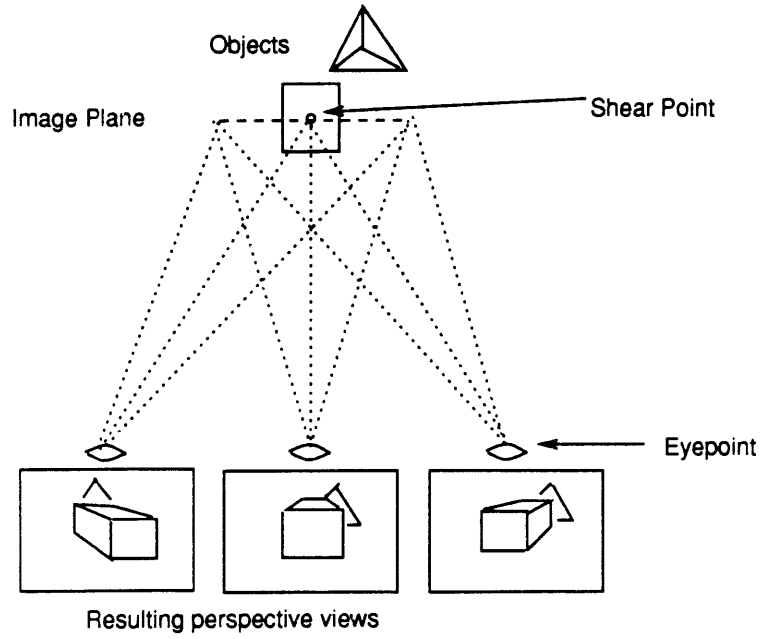
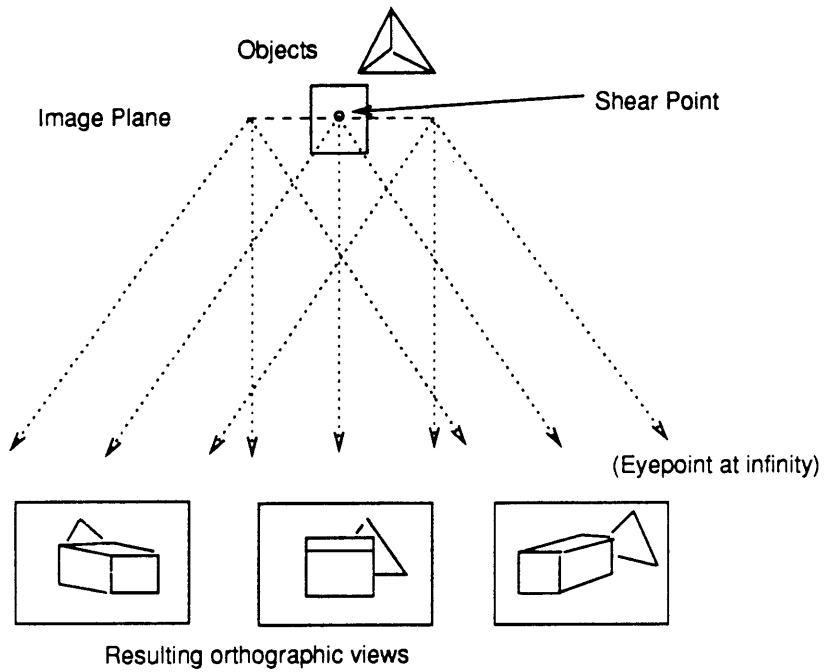


Figure 4.8: Renderer interface to holographic printer geometry.

PERSPECTIVE SHEARING WITH RECENTERING



ORTHOGRAPHIC SHEARING WITH RECENTERING



view distance = 50 cm.

(lensing equation (Benton, 1977))

view zone width = 39 cm.

(39 cm. = 100 views * .3 cm. each * 1.3 (horizontally magnified))

field of view = 28.48 degrees

$(28.48 = 2 * \text{atan} \left(\frac{(H2 \text{ width})/2}{\text{view distance}} \right))$

camera increment = $\frac{\text{view zone width}}{100 \text{ slits}}$

A sequence of 100 views is rendered using the resulting camera geometry. These views are color separated into their red, green and blue component images, and recorded on cine film.

Chapter 5: Holographic Display of Component Images

5.1 Mastering

Once all of the component views are recorded on cine film, the hologram master (H1) can be created. Because an animation of one hundred views was created, and each was color separated into its (R,G,B) component images, the H1 will be comprised of three hundred sub-holograms, each exposed as a 3mm-wide slit on the master plate. The mastering setup is shown in Figure 5.1.

Light from the laser is divided into two beams, one to reference the hologram, and the other to contain the object information. The reference beam is diverged and then collimated to illuminate the holographic plate one slit at a time. Simultaneously, the object beam is diverged and then condensed to illuminate each of the rendered, color-separated views that was recorded on 35mm cine film. The projection lens projects each of the rendered views onto a ground glass screen sequentially so that each exposed slit sees one of the 2D views.

In this manner, each of the one hundred rendered views is interfered with the reference

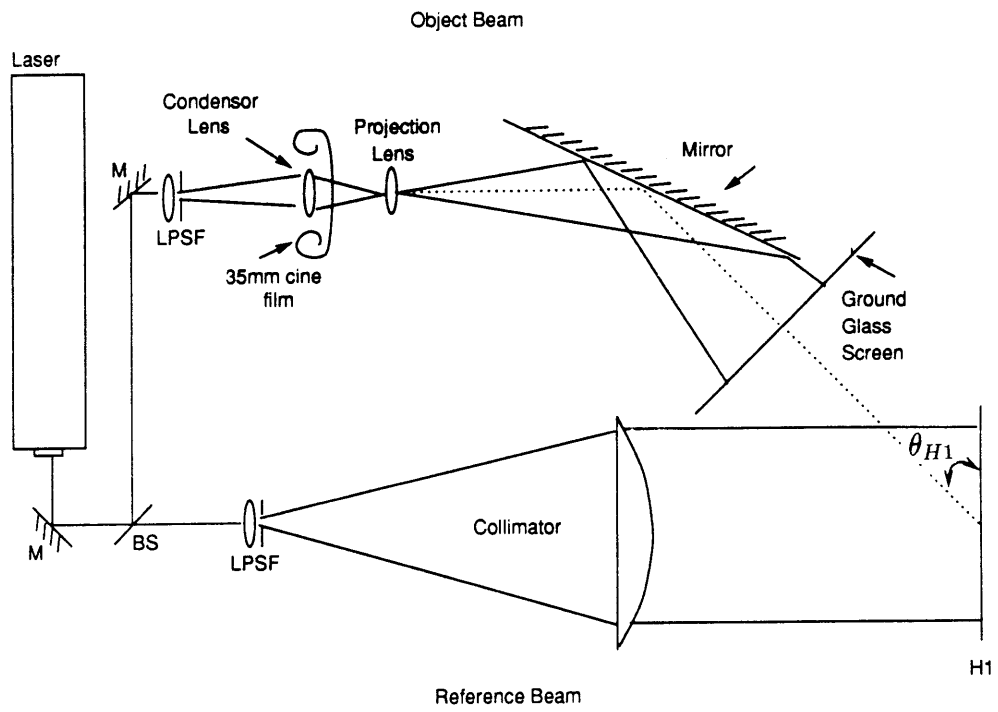


Figure 5.1: Stereogram master printer geometry.

beam and recorded sequentially on abutted vertical strips on the plate. Three recording passes are made, one for each of the animation color separations, with each sequence being exposed at a different location on the holographic plate.

In order to determine the locations on the H1 plate where each sequence of color separated images must be exposed, the following calculations, tailored specifically to the master, transfer and illumination setups are considered.

First, to achieve overlap, and on-axis alignment of corresponding red, green and blue color separations, spatial frequencies for wavelengths which mark transitions between blue and green wavelengths (500 nm), and between green and red wavelengths (590 nm), are calculated on axis. In the reconstruction, with the illumination source positioned at angle θ_{ill} , and with ($\theta_{out} = 0$), using the following for each λ ,

$$\sin\theta_{ill} - \sin\theta_{out} = \lambda f,$$

the spatial frequencies f_{500nm} and f_{590nm} are found.

Next, in the transfer setup, using the reference beam angle θ_{ref} , the angles to the transitions between the blue and green, $\theta_{obj500nm}$, and the green and red masters, $\theta_{obj590nm}$,

need to be determined. Using the spatial frequencies found above, and the fact that

$$\sin\theta_{obj} - \sin\theta_{ref} = \lambda_{laser} f,$$

the angles $\theta_{obj500nm}$ and $\theta_{obj590nm}$ are found.

From Figure 5.2, where the distance between the master and transfer plates is S , and the angle between the two planes is α , the distance of the transition points from the H1 center can be determined. Using the fact that

$$h = d\sin\alpha$$

and

$$D = S - d\cos\alpha$$

and also that

$$\tan\theta_{obj} = \frac{h}{D},$$

with the angles $\theta_{obj_{500nm}}$ and $\theta_{obj_{590}}$, the distances d_{500nm} and d_{590nm} can be determined. These distances specify that the green components of the color separated animation are recorded in the center of the plate, in a section (100 slits * 3mm wide), and ($d_{500nm} + d_{590nm}$) high (Figure 5.2). Likewise, the red component images are recorded below the green, and the blue ones are recorded above the green. Thus, the master holographic stereogram of a full-color sequence of images consists of 300 exposures, recorded in three separate horizontal bands of 100 vertical slits.

5.2 Transferring

After a hologram master is recorded, a flat-format transmission transfer is made of the H1 using the setup in Figure 5.3. The H1 is illuminated with the conjugate of the reference beam in the previous setup. The distance between the master and transfer plates is S , and the angle between the plates is α , both as used in the calculations above. A real image is projected out into the plane of the H2 such that the image is focused on the holographic plate. The H2 is referenced with a diverging beam at the angle θ_{ref} .

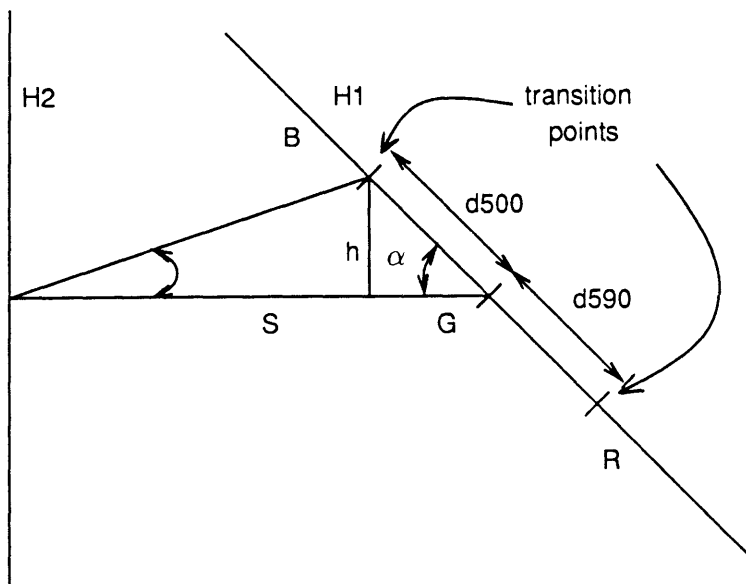


Figure 5.2: Locations of red, green and blue separations on $H1$.

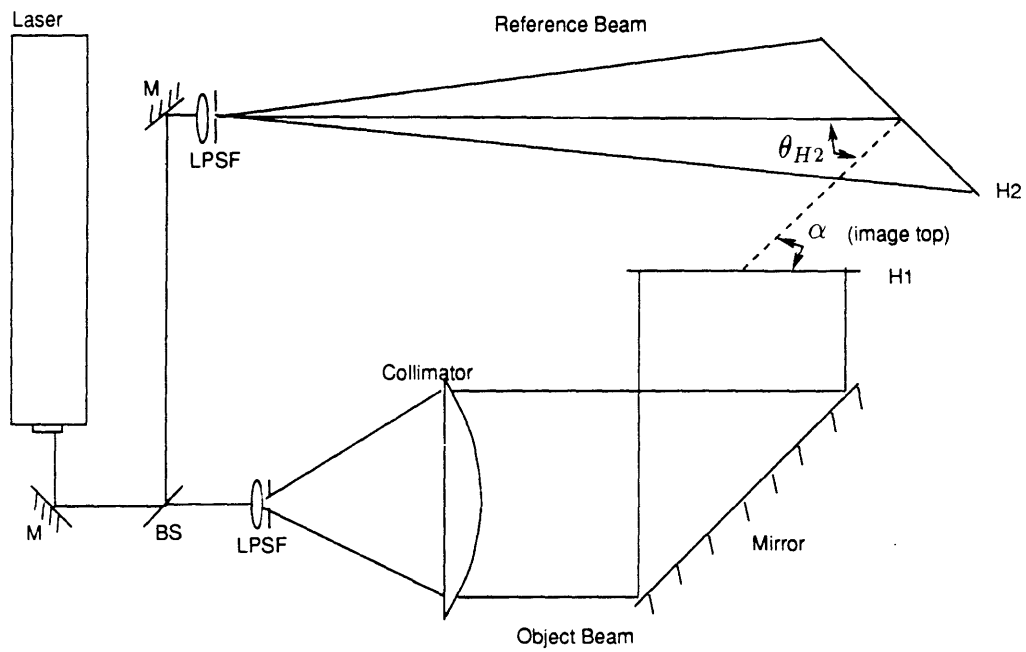


Figure 5.3: Holographic transfer printer geometry.

5.3 Reconstruction

The transmission rainbow hologram is viewable in white light, and the image is reconstructed as shown in Figure 5.4.

The H2 is illuminated at the angle θ_{ill} by a point or vertical line source of white light from the direction opposite to that of the beam used to reference the hologram in the transfer geometry. When the viewer's eyes are positioned along the equator of the hologram where the images of each color-separated sequence overlap, a full-color three-dimensional image can be seen. With vertical movement through the view zone, the color shift characteristic of rainbow holography is evident. As the viewer moves his eyes above the equator, he can begin to see only the blue component of the sequence reconstructing in the longer wavelengths, and movement below the center of the hologram shows the red component of the sequence reconstructing in shorter wavelengths. With horizontal eye movement throughout the viewing zone, where the image of the master hologram is focused, the viewer's eyes sweep through the side-to-side views, and the perception of the computer graphic image in three-dimensions is achieved.

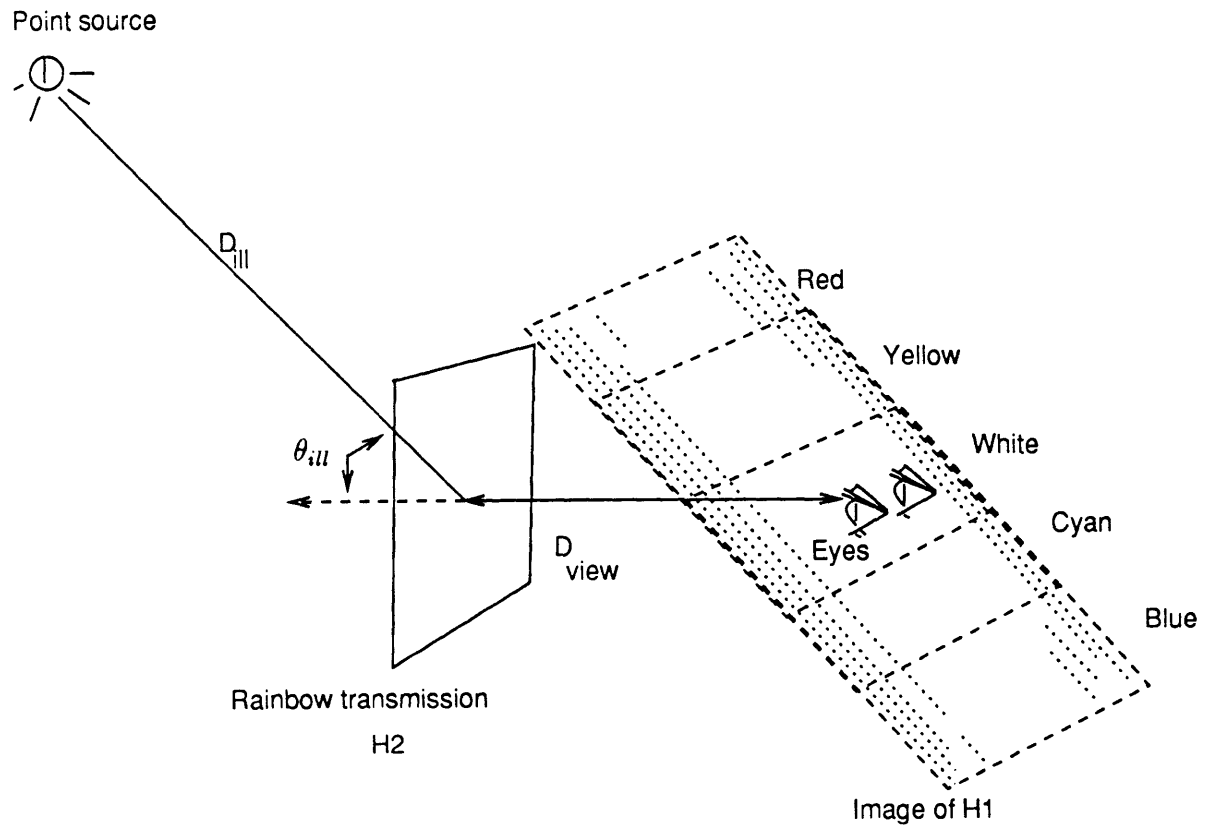


Figure 5.4: Reconstruction of the hologram.

Chapter 6: Results

6.1 Orthopedic CT

The first hologram generated using volumetric rendering and the holographic setups described was of the upper portion of a child's skull. Thirteen transverse CT slices with the resolution shown in Figure 6.1 constituted the initial data set, with each voxel value represented by 16 bits.

In order to obtain voxels that were a more isotropic representation of the data, additional slices were interpolated between each pair of originals. The interpolated data set consisted of 113 planes of voxels ($1\text{mm} * 0.8\text{mm} * 0.8\text{mm}$) in dimension.

Next, the planes were reoriented, so that new data files would be parallel to the image plane. In this orientation, a ray traveling in a straight line from an eyepoint looking at the front of the skull would intersect all data planes. The entire volume was cropped to eliminate many voxels which did not include data. The final volume size was (70 planes * 180 pixels * 113 pixels). Visual inspection of the individual slices lead to a decision *not* to attempt enhancement or filtering of the data. A histogram plot of the data set is shown

Slice position and spacing	rows (# voxels)	columns (# voxels)	voxel x res	voxel y res
-1 mm	320	320	0.8 mm	0.8 mm
3 mm } 4 mm	320	320	0.8 mm	0.8 mm
8 mm } 5 mm	320	320	0.8 mm	0.8 mm
13 mm } 5 mm	320	320	0.8 mm	0.8 mm
18 mm } 5 mm	320	320	0.8 mm	0.8 mm
22 mm } 4 mm	320	320	0.8 mm	0.8 mm
32 mm } 10 mm	320	320	0.8 mm	0.8 mm
42 mm } 10 mm	320	320	0.8 mm	0.8 mm
52 mm } 10 mm	320	320	0.8 mm	0.8 mm
62 mm } 10 mm	320	320	0.8 mm	0.8 mm
72 mm } 10 mm	320	320	0.8 mm	0.8 mm
82 mm } 10 mm	320	320	0.8 mm	0.8 mm
92 mm } 10 mm	320	320	0.8 mm	0.8 mm

Figure 6.1: CT head scan data set.

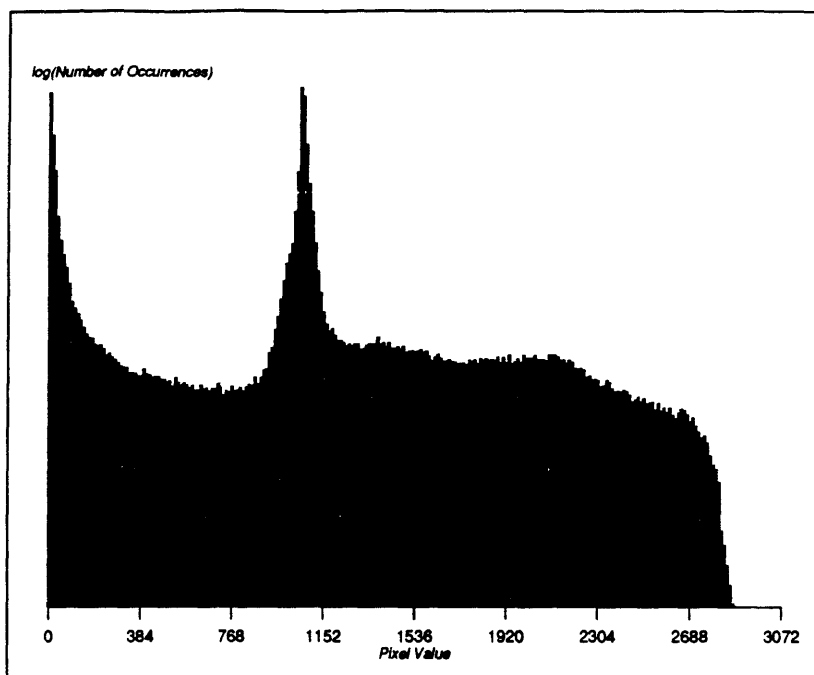


Figure 6.2: Histogram plot of CT head data set.

in Figure 6.2. The motivation for this experiment was to produce a three-dimensional image of the bones in the volume. It was an easy task to locate the bone in the data set, within a tissue density window of 1300 to 3000.

A grayscale to opacity mapping of

grayscale

opacity

0	0.0
1200	0.0
1300	1.0
3000	1.0
4000	0.0

was selected for voxel opacity assignment, and both gradient and opacity volumes were then calculated. Illumination parameters specifying ambient light, surface diffusivity and specularity assigned to the bone tissue, and light source color are given below.

$$KA = 0.0025$$

$$KD = 0.15$$

$$KS = 0.9$$

$$c_{l_1} = (1.0, 0.95, 0.7)$$

In addition, the background color was initialized to be $c_{backg} = (0.78, 0.3, 0.68)$.

An animation of one hundred views was computed on a Gould PN9000, at an expense of 55 minutes/frame. Resulting frames were sized (180 pixels wide * 113 pixels high),

so additional background was added on all sides of each frame to extend their dimension to (320 * 240) pixels. These images were then interpolated to the size of the frame buffer used, (640 * 480 pixels) (Figure 6.3), color separated, and then recorded onto cine film. The hologram was mastered, and a white light rainbow transfer was made (8" high * 10" wide * 8" apparent depth) which provides an excellent visualization of the skull in three dimensions. Even though the original data slices were five to ten millimeters apart, the image conveys the structure of the skull very well despite this low resolution (Figure 6.4).

6.2 Cardiac MRI

The donation of MRI data of an *in vitro* beef heart provided the opportunity to examine MRI as a source of volumetric data. Two experiments were conducted using this data, one based on imaging the heart sliced in half as a solid, opaque tissue, and the other based on investigating its display as partially transparent tissue.

The data volume donated consisted of 108 data files, each (115 pixels wide * 200 pixels high). Since the data set came with no intraplane or interplane spatial resolution specifications, the final dimensions of the heart had to be estimated. To compensate for an incorrect aspect ratio, each plane of data was interpolated from 115 to 175 pixels wide. In addition, one additional plane was interpolated between each two original data planes. This provided a volume of data sized 216 planes * 200 pixels * 175 pixels.

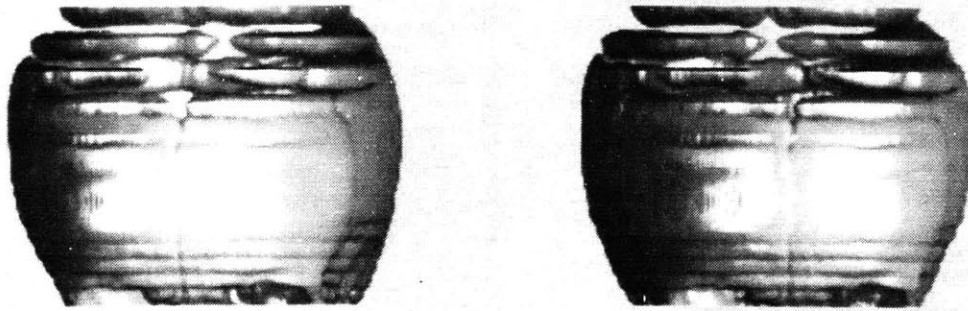


Figure 6.3: Computer graphically reconstructed images of child's skull.

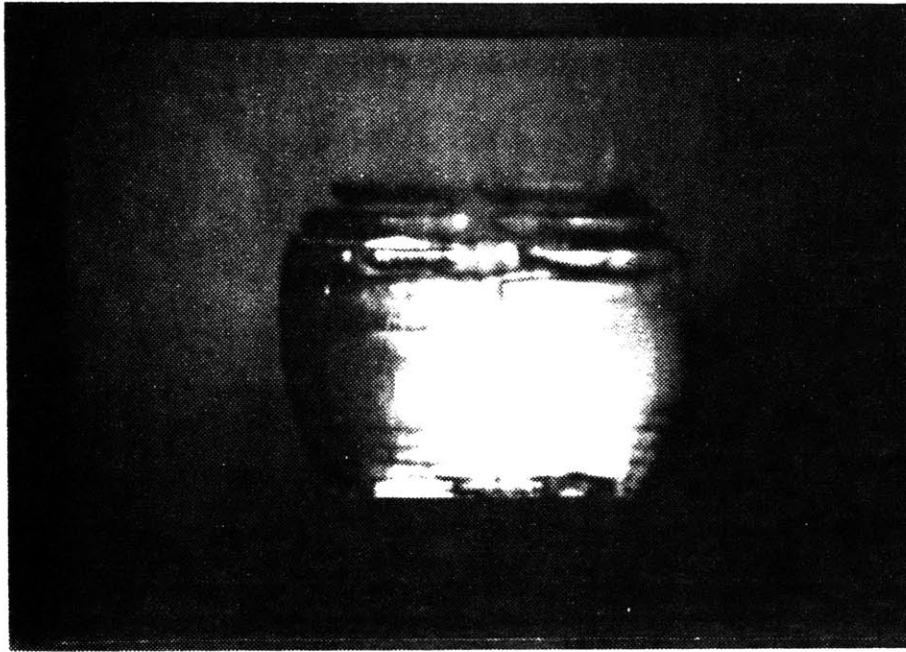


Figure 6.4: Hologram of child's skull.

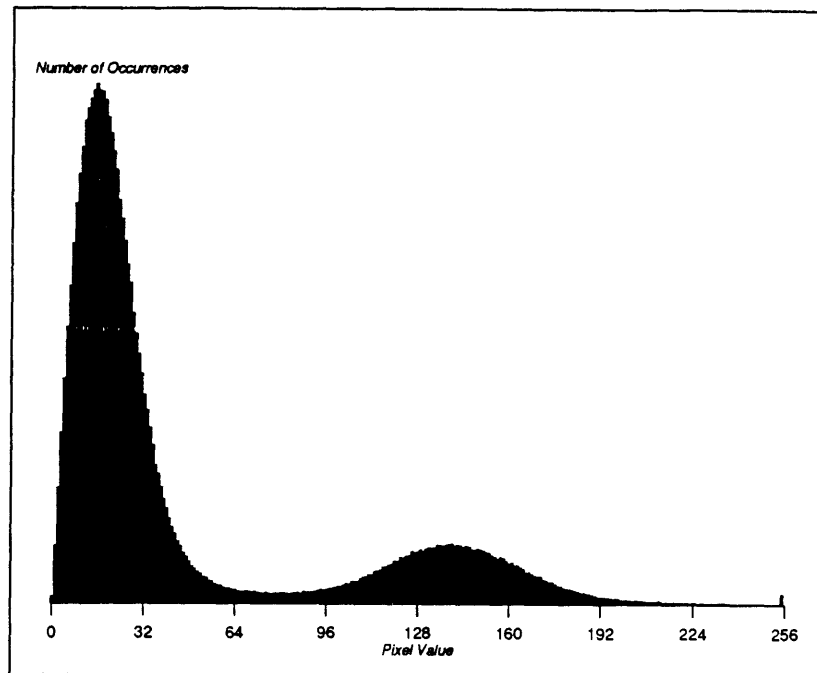


Figure 6.5: Histogram plot of MRI heart data set.

Because the data was also very noisy, mostly as a result of shot noise and magnetic field inhomogeneities, a 2D low pass filter was applied to all files in the volume before calculating the gradients. These files constituted the set of data from which the final images were rendered. A histogram plot of the data set is shown below in Figure 6.5.

6.2.1 Opaque Heart

Only data files from the back half of the data volume were used to provide an image of a long-axis section through the heart. The grayscale to opacity mapping below was chosen to render the tissue opaquely.

grayscale	opacity
0	0.0
80	0.0
90	0.5
100	1.0
255	1.0

This mapping effectively attenuated the ambient noise in the air surrounding the tissue.

Next, using the a portion of the data files sized 99 planes * 200 pixels * 175 pixels, the gradient and opacity volumes were generated. Surface parameters were assigned to the heart tissue,

$$KA = 0.0025$$

$$KD = 0.2$$

$$KS = 0.95$$

and three light sources with colors and positions as below,

$$c_{l_1} = (0.75, 0.08, 0.08)$$

$$c_{l_2} = (0.6, 0.09, 0.09)$$

$$c_{l_3} = (0.6, 0.09, 0.09)$$

$$\text{pos}_{l_1} = (-50.0, -100.0, 0.0)$$

$$\text{pos}_{l_2} = (50.0, -100.0, 0.0)$$

$$\text{pos}_{l_3} = (0.0, -100.0, 0.0)$$

and the final image was initialized to have $c_{backg} = (0.66, 0.66, 0.66)$.

Again, an animation of one hundred views was computed on a Gould PN9000 with each view taking 65 minutes to render. The resulting rendered frames were sized 200 * 175 pixels, so additional background was added on all sides of the images to yield 240 * 320 pixel images. These images were then interpolated to produce the final set of one hundred 480 * 640 pixel frames (Figure 6.6), which were color separated, and then recorded on cine film.

A hologram was mastered, and a white light rainbow transfer (8" high * 10" wide * 4" apparent depth) was made. The reconstructed image, which was colored primarily red, imposed a restriction on the viewer to be at the color focus (about 19 inches from the plate). Since the amount of information in the green and blue color separations was small, the image was not very informative to a viewer outside the color focus.

Since this restriction was quite unsatisfactory, the red separation was remastered, and a full aperture transfer produced an achromatic image which provided a good three-

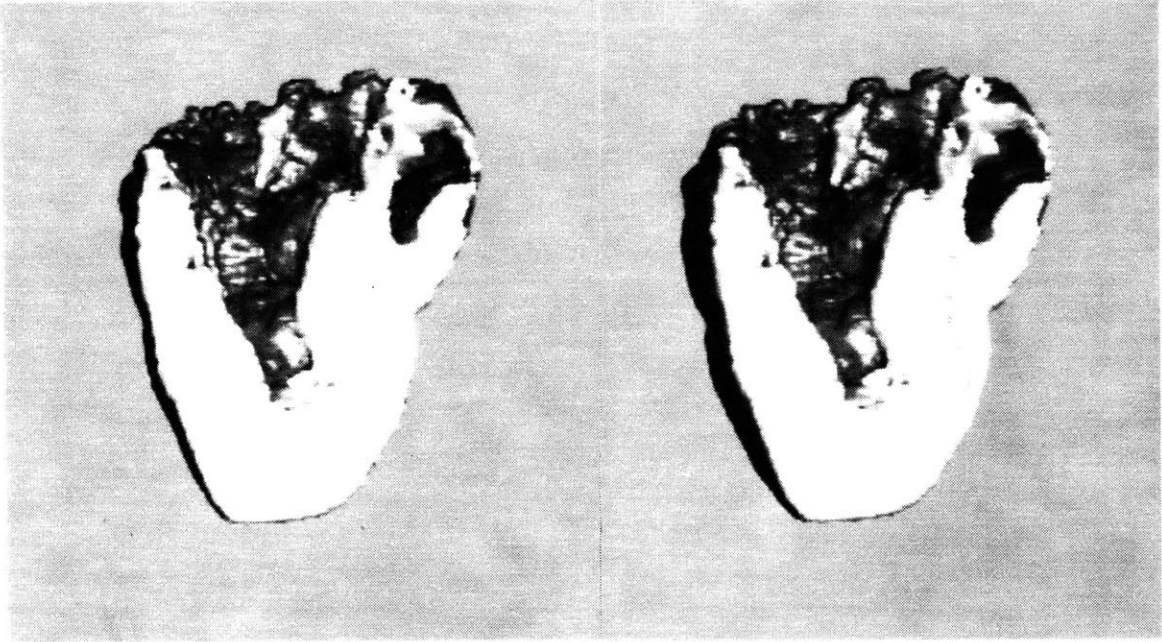


Figure 6.6: Computer graphically reconstructed images of opaque heart.

dimensional visualization of the long-axis section of the beef heart (Figure 6.7).

The next experiment included the rendering of the entire heart data set with a larger degree of transparency. Since using the entire heart volume represented a considerable increase in data to be rendered and computation time was already expensive, much time was spent optimizing the software to render more efficiently. With the new changes in the software, time required to render from a volume of 99 planes * 200 pixels * 175 pixels illuminated by three light sources went from 65 minutes/frame to 28 minutes/frame.

6.2.2 Transparent Heart

The same set of interpolated, low pass filtered data was used to render the transparent heart. The goal of this experiment was to compare still images, animations providing kinetic depth, and true 3D representations of a partially transparent object with regard to comprehensibility and information content.

A grayscale to opacity mapping was constructed as below.

grayscale	opacity
0	0.0
80	0.0
90	0.0015



Figure 6.7: Hologram of long-axis section of a beef heart.

255

0.0015

Gradient and opacity volumes were computed for a data volume comprised of 175 slices * 200 pixels * 175 pixels. The rendering of an animation of 100 images was computed using tissue surface parameters,

$$KA = 0.0025$$

$$KD = 0.2$$

$$KS = 0.9$$

and three light sources with colors and positions as below,

$$c_{l_1} = (1.0, 1.0, 1.0)$$

$$c_{l_2} = (1.0, 1.0, 1.0)$$

$$c_{l_3} = (1.0, 1.0, 1.0)$$

$$pos_{l_1} = (-50.0, -100.0, 0.0)$$

$$pos_{l_2} = (50.0, -100.0, 0.0)$$

$$pos_{l_3} = (0.0, -50.0, 0.0)$$

The resulting images were not as effective as was hoped, and the desired comparisons between 2D and 3D presentations could not be made. Spurious tissue interiors reflected light since distinctions between translucent tissue surfaces and tissue interiors were not as obvious as was anticipated (Figure 6.8). Presumably, noisy gradient vectors within tissue interiors resulting from data noise, were indicating surfaces where none existed.

A test of this assumption was performed on a noiseless, binary-valued data volume created as shown in Figure 6.9. The gradient volume was computed as well as an opacity volume that mapped byte value 255 to transparency value 0.08. A view rendered from an eyepoint directly on the y-axis, with illumination directly behind the eye, showed that surfaces **A** and **B** reflected light and that the interior of the subvolume V_2 was invisible, as expected.

From these investigations came the conclusion that transparently rendered soft tissues of secondary importance can aid comprehension of the data when presented with the more opaque object of interest. However, using the image filtering and rendering techniques examined in this work, transparent objects of primary interest fail to provide enough structural information to the viewer.

Best results were obtained with CT data, and images of bone tissue, since it is so easily identified. More experimentation, however, with methods of smoothing MRI data

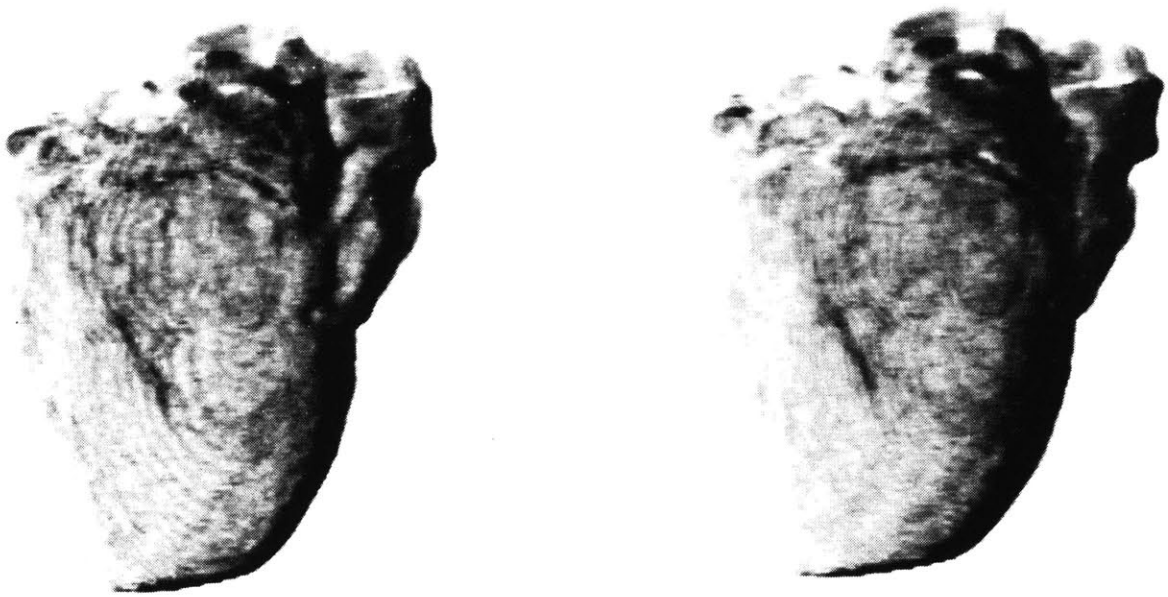


Figure 6.8: Computer graphically reconstructed images of transparent heart.

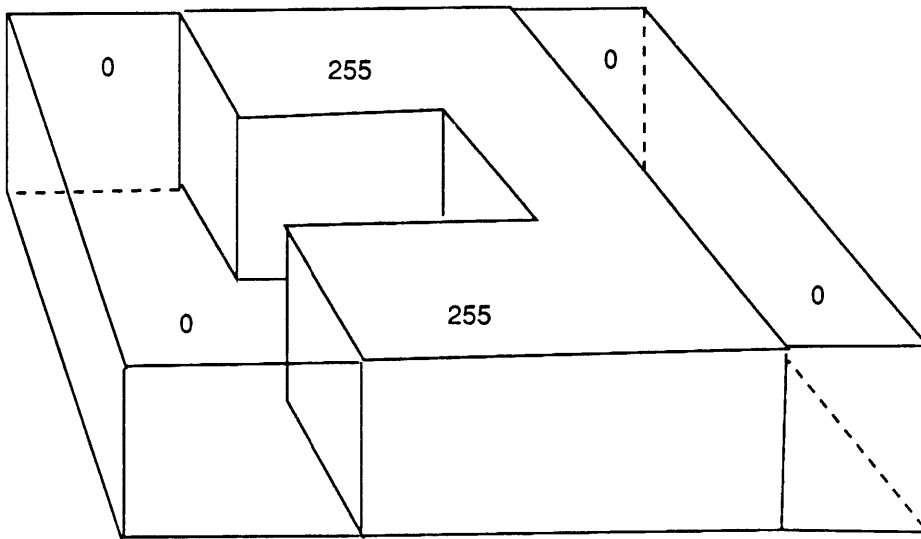


Figure 6.9: Test volume.

without degrading surface detail is necessary. In addition, a method of assigning opacities to tissue types more compatible to MRI is desirable.

6.3 Image Quality

Although the images created from the CT scans of the child's skull provided a good visualization of bone tissue from the coarsely-scanned data, it is also illustrative of a few ways in which image quality may be improved. For example, the silhouette edges of the bone are sharp and abrupt. Levoy mentions that blurring the array of acquired CT values in the preprocessing step can soften these oversharped surface silhouettes. Indeed, when the initial CT data of the skull was obtained, the only criterion used to ascertain the need for filtering was the presence of noise within the data. Since all slices appeared to have an acceptable level of noise, no smoothing was performed on the set. In addition, such filtering may have helped blend the interplane slices more gradually, softening the "sliced" look of the image.

Another way to minimize the "sliced" look of the image is to apply 3D filtering techniques to the gradient volume. A simple averaging filter (Figure 6.10) applied to the gradients has the effect of smoothing the surfaces [Troussset and Schmitt, 1987]. A window sized three or five voxels on a side can be convolved with the gradient volume in a preprocessing step to yield a smoothed gradient volume.

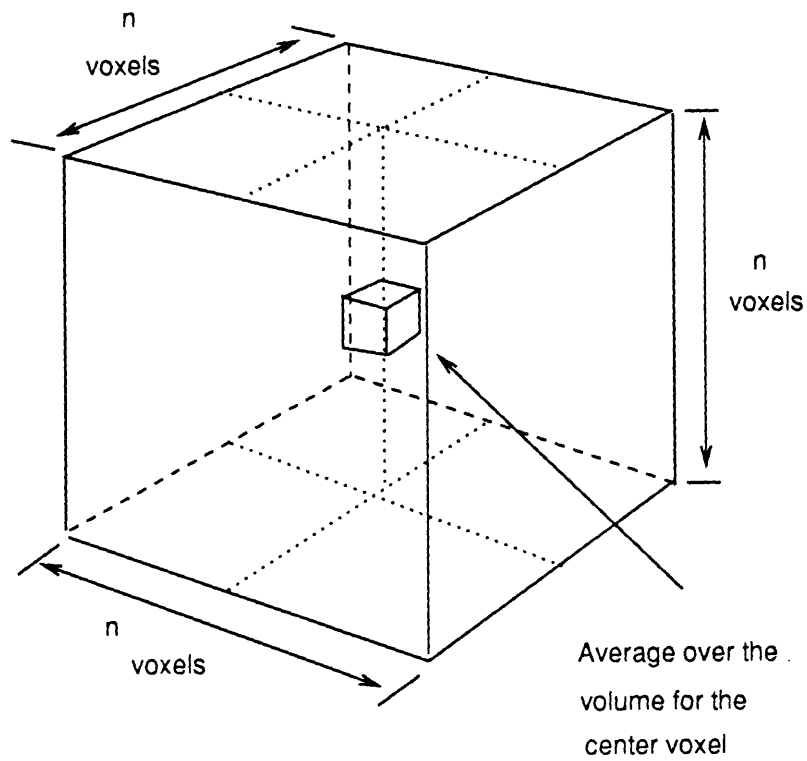


Figure 6.10: 3D averaging filter.

Though the data slices are less obvious in the surfaces rendered using the smoothed gradients, the surfaces tend to look blurred. Although slightly blurry surfaces are not necessarily a problem, applying the same filtering techniques to the opacity volume rather than the gradient volume preserves surface detail, while softening harsh boundaries between tissues.

A more obvious rendering artifact arose in the sequence of frames generated of the transparent heart. In these frames, the structure of the original slices, which were oriented parallel to the image plane, was evident in *some* of the images as light was reflected to the eye from their stair-step structure at only some of the eyepoint locations. This effect proved to be quite kinetic as the eyepoint moved and, as a result represented a major distraction to the viewer.

If original scans taken with a finer interplane resolution are used, then the resulting surfaces do not reflect the scan structure as much. In addition, if slices in the volume are oriented to be orthogonal rather than parallel to the image plane, then the slice structure will be vertical and thus equally obvious from all viewpoints. This orientation prevents the annoying “popping in and out” of the differentiation between slices.

Another way of increasing visibility is to supersample along each ray. For each sequence of images generated in this work, two sample points were considered per voxel. The improvement in image quality offered by this resolution over tests done with one sample point per voxel was considerable. Although increasing the sampling rate does improve

image quality, it also adds to the time required to compute each frame. Sampling each voxel more than twice marked the point at which image enhancement no longer outweighed the extra computation time required to evaluate more samples.

Chapter 7: Conclusions and Future Work

Imaging modalities such as CT and MRI generate a volume of diagnostic imaging data that requires efficient and precise evaluation. It is possible that holography might contribute to such evaluation in future imaging systems. The coupled use of volumetric editing and rendering and holographic stereogram technology provided superior visualization of surfaces in three dimensions.

This work has attempted to demonstrate that spatial display offers a clearly understandable representation of the complex structures present in medical data. Holographic stereograms of volume rendered images incorporate all of the advantages of 3D editing and reconstruction of tissue as well as the perceptual benefits of spatial display in hard-copy form. As familiarity with this technology grows among the medical community, it is expected that more applications to which holography is well-suited will emerge.

The next logical research step should be the recording of holographic images that combine opaque tissues of interest with more transparent surrounding tissue. In such an image, none of the data contained in the data volume would be completely suppressed.

The resulting hologram would display *all* of the information available in the volume, yet tissues of primary interest would not be overwhelmed by subordinate ones. In addition, comparisons could be made between monocular and binocular perceptions of transparent tissue.

Reaction to these holographic images by the medical professionals questioned was positive, yet cautious. The considerable time involved in generating such an image from the original scan data does not yet approach the necessarily minimal production time which might allow a 3D hardcopy to be a useful tool. In addition, the lack of vertical parallax was noted and found to be a distraction due to the desire to evaluate the three-dimensional image from many more vantage points than were actually computed. Furthermore, narrow holographic viewing zones limit the size of viewing audiences. Ideally, many clinicians should be able to view a holographic stereogram concurrently from different viewpoints. Overall response to the holographic images, however, remains supportive of further work in this area.

The issues mentioned above are among those that will need to be addressed as work on holographic stereograms displaying medical data continues. Improvements in holographic technology must occur in conjunction with further developments in 3D image processing and rendering of volumetric data.

References

Benton, S. A., "'Alcove' Holograms for Computer-Aided Design", SPIE Proc. #761, "True 3-D Imaging Technologies and Display Technologies", January, 1987.

Benton, S. A., "Prospects for quasi-holographic three-dimensional displays in the biomedical sciences", *Holography in Medicine*, Proceedings of the International Symposium on Holography in Biomedical Sciences, New York, 1973.

Benton, S. A., "White-Light Transmission/Reflection Holographic Imaging", E. Marom and A. A. Friesem eds., *Applications of Holography and Optical Data Processing*, Pergamon Press, Oxford, 1977, pp. 401-409.

Benton, S. A., "Survey of holographic stereograms", SPIE Vol. 367, *Processing and Display of Three-Dimensional Data*, 1982.

Blinn, J., "Light Reflection Functions for Simulation of Clouds and Dusty Surfaces", ACM SIGGRAPH, 1982.

Cornsweet, T., *Visual Perception*, Academic Press, 1970.

Drebin, R. A., Carpenter, L., Hanrahan, P., "Volume Rendering", (to be published at SIGGRAPH 1988).

Eskridge, J. M., Lacey, D. C. L., Gilmor, R. L., Klatte, E. C., "Holographic Cerebral Angiography Using Image Plane Integral (IPI) Holography", Prepared for exhibition at the annual meeting of The American Society of Neuroradiology, Feb. 18-23, 1985.

Fuchs, H., Kedem, Z. M., Uselton, S. P., "Optimal surface reconstruction from planar contours", *Communications of the ACM*, 20(10), 1977, 693-702.

Fujioka, M., Ohyama, N., Honda, T., Tsujiuchi, J., Suzuki, M., Hashimoto, S., Ikeda, S., "Holography of 3D Surface Reconstructed CT Images", *Journal of Computer Assisted Tomography*, 12(1): 175-178, January/February 1988.

Groh, G., Kock, M., "3D Display of X-Ray Images by Means of Holography", *Applied*

Optics, Vol. 9, No. 3, March 1970.

Hohne, K. H., Bernstein, R., "Shading 3D Images from CT Using Gray-Level Gradients", IEEE 1986.

Hoppenstein, R., "Three-Dimensional time sequence radiography, a quasi-holographic technique", *Holography in Medicine*, Proceedings of the International Symposium on Holography in Biomedical Sciences, New York, 1973.

Kulick, J., Halle, M., "Volumetric Display of Soft Tissue Via Holography", SPIE, Medical Imaging II, 1988.

Lacey, D. C. L., "Radiologic Applications of Holography", SPIE, Vol. 761, True 3D Imaging Techniques and Display Technologies, 1987.

Levoy, M., "Volume Rendering: Display of Surfaces from Volume Data", IEEE, May 1988.

Levoy, M., "Direct Visualization of Surfaces from Computed Tomography Data", SPIE, 1988.

Lorensen, W. E., Cline, H. E., "Marching Cubes: A High Resolution 3D Surface Construction Algorithm", ACM SIGGRAPH, 1987.

Okoshi, T. *Three-Dimensional Imaging Techniques*, Academic Press, Inc., 1976.

Pizer, S. M., Fuchs, H., "Three Dimensional Image Presentation Techniques in Medical Imaging", *Computer Assisted Radiology*, Proceedings of the International Symposium on Computer Assisted Radiology, 1987.

Tsujiuchi, J., Honda, T., Suzuki, M., Saito, T., Iwata, F., "Synthesis of Multiplex Holograms and Their Application to Medical Objects", SPIE Vol. 523 Applications of Holography, 1985.

Trousset, Y., Schmitt, F., "Active-Ray Tracing for 3D Medical Imaging", Eurographics '87,, 1987.

Vannier, M., Butterfield, R. L., Rickman, D. L., Jordan, D. M., Murphy, W. A., Biondetti, P. R., "Multispectral Magnetic Resonance Image Analysis", CRC Critical Reviews in Biomedical Engineering, Vol. 15, Issue 2, 1987.

Bibliography

Arnheim, R. *Art and Visual Perception*, University of California Press, 1974.

Bos, P., Johnson, P., Koehler, R., Tektronix, Inc., "A liquid-crystal optical-switching device (PI cell)," Proc. Soc. for Infor. Disp., 1983

Fishman, E. K., Magid, D., Ney, D., Drebin, R., Robertson, D., Scott, W., "Volumetric 3D Imaging of the Hip: Applications in Acetabular Fractures", *Computer Assisted Radiology*, Proceedings of the International Symposium on Computer Assisted Radiology, 1987.

Fishman, E., Magid, D., Ney, D., Drebin, R., Kuhlman, J., "Three-Dimensional Imaging and Display of Musculoskeletal Anatomy", *Journal of Computer Assisted Tomography*, 12(3) pp. 465-467, May/June, 1988.

Fishman, E., Magid, D., Ney, D., Drebin, R., Robertson, D., Scott, W. Jr., "Volumetric 3-D Imaging of the Hip: Applications in Acetabular Fractures", *Computer Assisted Radiology*, Proceedings of the International Symposium on Computer Assisted Radiology, 1987.

Foley & Van Dam, *Fundamentals of Interactive Computer Graphics*, Addison-Wesley, 1984

Grattoni, P., Pollastri, F., "A Contour Detection Algorithm Based on the Minimum Radial Inertia (MRI) Criterion", *Computer Vision, Graphics, and Image Processing*, 43, pp. 22-36, 1988.

Gregory, R. L., *Eye and Brain: The Psychology of Seeing*, McGraw-Hill, 1977.

Grimson, W., *From Images to Surfaces: A Computational Study of the Human Early Visual System*, MIT Press, 1981.

Halle, M., "Applications of Synthetic Holography in Medical Imaging", MIT BSCS Thesis, (1988).

Heffernan, P. B., Robb, R. A., "A New Method for Shaded Surface Display of Biological

- and Medical Images", IEEE Trans. on Med. Imaging, Vol. MI-4, No. 1, March 1985.
- Herman, G. T., Udupa, J. K., "Display of 3-D Digital Images: Computational Foundations and Medical Applications", IEEE Computer Society Press, pp. 308-314, 1983.
- Herman, G. T., "Three-Dimensional Imaging on a CT or MR Scanner", Journal of Computer Assisted Tomography, 12(3): pp. 450-458, May/June 1988.
- Hoffman, E. J., Phelps, M. E., "Positron Emission Tomography: Principles and Quantitation", Positron Emission Tomography and Autoradiography: Principles and Applications for the Brain and Heart, Raven Press, New York, 1986.
- Holzbach, M., "Three-Dimensional Image Processing for Synthetic Holographic Stereograms", MIT MS Thesis, (1981).
- Hoppenstein, R., "Three-Dimensional time sequence radiography, a quasi-holographic technique", *Holography in Medicine*, Proceedings of the International Symposium on Holography in Biomedical Sciences, New York, 1973.
- Hutzler, P., "Frequency Space Filtering of 3-D Voxel Images", *Computer Assisted Radiology*, Proceedings of the International Symposium on Computer Assisted Radiology, 1987.
- Lang, P., Steiger, P., Genant, H. K., Chafetz, N., Lindquist, T., "Three-Dimensional CT and MR Imaging in Congenital Dislocation of the Hip: Clinical and Technical Considerations" Journal of Computer Assisted Tomography, 12(3) pp. 459-464, May/June, 1988.
- McShan, D. L., Glickman, A. S., "Color Displays for Medical Imaging", Color and the Computer, Academic Press, Inc. 1987.
- Perlmutter, R., Friedland, S., "Computer-Generated Holograms in Biology and Medicine", IEEE, 1983.
- Porter, T., Duff, T., "Compositing Digital Images", Computer Graphics, Volume 18, Number 3, July 1984.
- Raafat, H. M., Wong, A. K. C., "A Texture Information-Directed Region Growing Algorithm for Image Segmentation and Region Classification", Computer Vision, Graphics, and Image Processing, 43, pp 1-21, 1988.
- Robb, W., "Future Advances and Directions in Imaging Research", AJR 150:39-42, January 1988 .

Rogers, B., Graham, M., "Similarities Between Motion Parallax and Stereopsis in Human Depth Perception", *Vision Research*, Vol. 22, pp. 261-270, 1982.

Serpico, S., Vernazza, G., Dellipiane, S., "Surface-Preserving Smoothing in 3-D NMR Imaging", *Computer Assisted Radiology*, Proceedings of the International Symposium on Computer Assisted Radiology, 1987.

Smith, W. K., Schlüsselberg, D., Woodward, D., "Algorithms for Ray-Tracing Volumetric Representations of Medical Image Data", *Computer Assisted Radiology*, Proceedings of the International Symposium on Computer Assisted Radiology, 1987.

Stevens, K. A., Brookes, A., "Integrating Stereopsis with Monocular Interpretations of Planar Surfaces", *Vision Research*, Vol. 28, No. 3, pp. 371-386, 1988.

Vannier, M., Butterfield, R. L., Rickman, D. L., Jordan, D. M., Murphy, W. A., Biondetti, P. R., "Multispectral Magnetic Resonance Image Analysis", *CRC Critical Reviews in Biomedical Engineering*, Vol. 15, Issue 2, 1987.